DISSERTATIONS IN
FORESTRY AND
NATURAL SCIENCES

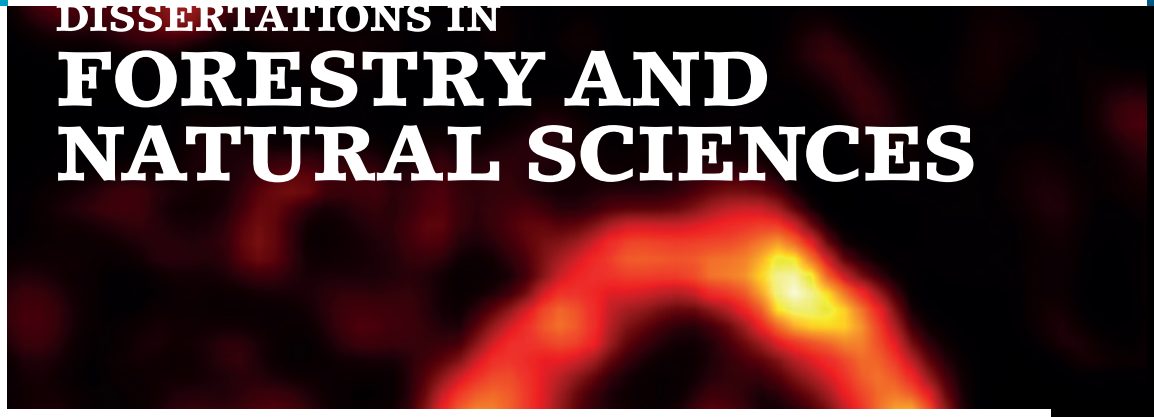

Tuomas Koivumäki

The Bioimpedance Technique in Respiratory- and Dual-Gated Positron Emission Tomography Imaging

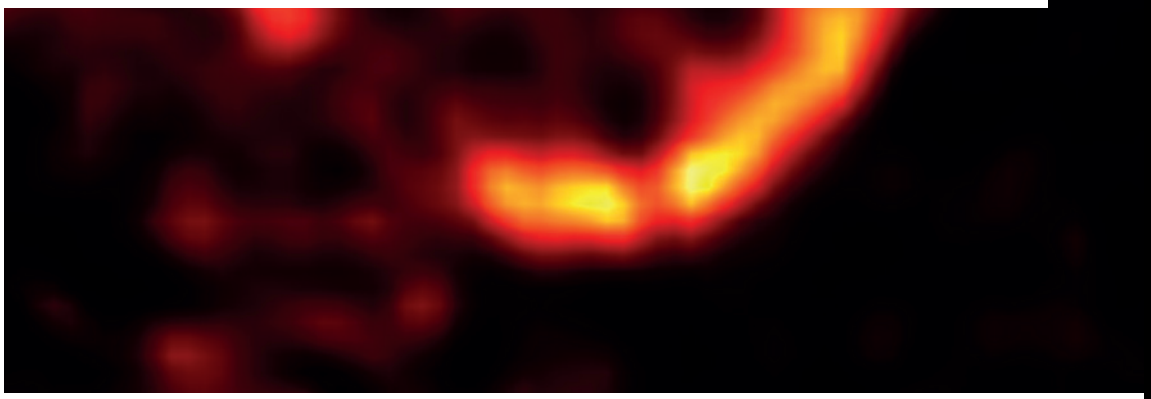

Publications of the University of Eastern Finland
Dissertations in Forestry and Natural Sciences

UNIVERSITY OF
EASTERN FINLAND

TUOMAS KOIVUMÄKI

The Bioimpedance Technique in Respiratory- and Dual-Gated Positron Emission Tomography Imaging

Publications of the University of Eastern Finland
Dissertations in Forestry and Natural Sciences
No 158

Academic Dissertation
To be presented by permission of the Faculty of Science and Forestry for public examination in the Auditorium MS302 in Medistudia Building at the University of Eastern Finland, Kuopio, on October, 17, 2014, at 12 o'clock noon.

Diagnostic Imaging Centre, Kuopio University Hospital
Department of Applied Physics

Grano Oy
Kuopio, 2014
Editors: Prof. Pertti Pasanen,
Prof. Pekka Kilpeläinen, Prof. Kai Peiponen, Prof. Matti Vornanen

Distribution:
Eastern Finland University Library / Sales of publications
P.O.Box 107, FI-80101 Joensuu, Finland
tel. +358-50-3058396
http://www.uef.fi/kirjasto

ISBN: 978-952-61-1580-1 (printed)
ISBN: 978-952-61-1581-8 (PDF)
ISSNL: 1798-5668
ISSN: 1798-5668
ISSN: 1798-5676 (PDF)

Author's address: Kuopio University Hospital
Cancer Center
P.O.Box 100
70029 KYS
FINLAND
email: tuomas.koivumaki@kuh.fi

Supervisors: Professor Marko Vauhkonen, Ph.D.
University of Eastern Finland
Department of Applied Physics
P.O.Box 1627
70211 KUOPIO
FINLAND
email: marko.vauhkonen@uef.fi

Adjunct Professor Mikko Hakulinen, Ph.D.
Kuopio University Hospital
Diagnostic Imaging Centre
P.O.Box 100
70029 KYS
FINLAND
email: mikko.hakulinen@kuh.fi

Adjunct Professor Esko Vanninen, M.D., Ph.D.
Kuopio University Hospital
Clinical Support Services
P.O.Box 100
70029 KYS
FINLAND
email: esko.vanninen@kuh.fi

Reviewers: Professor Hannu Eskola, Ph.D
Tampere University of Technology
Department of Electronics and Communications Engineering
P.O.Box 527
30101 TAMPERE
FINLAND
email: hannu.eskola@tut.fi

Ralph Bundschuh, M.D., Ph.D.
Universitätsklinikum Bonn
Klinik und Poliklinik für Nuklearmedizin
Sigmund-Freud-Straße 25
53127 BONN
GERMANY
email: ralph.bundschuh@ukb.uni-bonn.de

Opponent:

Professor Brian Hutton, Ph.D.
University College London
Institute of Nuclear Medicine
level 5 UCH
235 Euston Road
LONDON
UNITED KINGDOM
email: b.hutton@ucl.ac.uk

ABSTRACT

Respiratory and cardiac motion artefacts degrade image quality in positron emission tomography (PET) imaging and may significantly affect the qualitative and quantitative evaluation of images. At worst, misguided interpretation may lead to wrong diagnosis and inadequate or unnecessary treatment. The aim of this thesis was to study the feasibility of the bioimpedance-based measurement technique for respiratory and cardiac motion compensation in PET imaging.

An optimized bioimpedance measurement configuration for simultaneous measurement of respiratory and cardiac gating signals was first determined based on computational modelling. The configuration was further validated against reference methods for monitoring respiration and cardiac contractions. The feasibility of bioimpedance techniques for gating in clinical settings was evaluated in oncologic and cardiac PET studies.

Respiratory and cardiac bioimpedance measurements were found to have a high degree of correlation and good agreement with reference methods in monitoring respiration and cardiac contractions. In oncologic PET studies, bioimpedance-based respiratory gating resulted in a significant increase of the observed metabolic activity of lesions and a decrease of their volume. In cardiac PET studies, dual gating was found to show a significant narrowing effect on the observed myocardial wall thickness compared to plain cardiac gating.

This thesis shows that bioimpedance techniques can be effectively utilized for respiratory motion compensation by respiratory and dual gating of PET imaging. Further development of bioimpedance-based respiratory motion compensation should be mainly directed to enhancing the sensitivity and linearity of the measurement configuration.

National Library of Medicine Classification: QT 36, WF 141, WG 141.5.T6, WN 180, WN 206

Medical Subject Headings: Diagnostic Imaging/methods; Electric Impedance; Sensitivity and Specificity; Image Enhancement; Artifacts; Positron-Emission Tomography; Respiratory System; Respiratory-Gated Imaging Techniques; Heart; Cardiac-Gated Imaging Techniques; Neoplasms

Yleinen suomalainen asiasanasto: kuvantaminen; positroniemissiotomografia; bioimpedanssi; artefaktit; liikkeet; kompensointi; kuvanlaatu; hengityselimet; sydän; kasvaimet

Acknowledgments

The studies presented in this thesis were carried out at the Department of Applied Physics, University of Eastern Finland, and the Department of Clinical Physiology, Nuclear Medicine and Clinical Neurophysiology, Kuopio University Hospital, during 2009-2014. Part of this thesis was done in Turku PET Centre, Turku University Hospital, in 2012, and the Department of Nuclear Medicine, Technische Universität München, in 2013. I wish to take this opportunity to thank all those who have contributed to my studies and supported my work toward this thesis. In particular, I wish to express my gratitude to the following persons.

First of all, I want to thank my supervisors Professor Marko Vauhkonen, Ph.D., Adjunct Professor Mikko Hakulinen, Ph.D., and Adjunct Professor Esko Vanninen, M.D., Ph.D., for their expert guidance as well as their never-ending ability to give valuable advice and encouragement during this work.

I thank the official reviewers Professor Hannu Eskola, Ph.D., and Ralph Bundschuh, M.D., Ph.D., for their constructive criticism and invaluable suggestions to improve this thesis. I am also grateful to Gerald G Netto, Ph.D., for revising the language of this thesis.

I warmly thank all the co-authors of the original publications for their significant contribution. I want to especially thank Professor Jyrki Kuikka, Ph.D., for guiding me to the world of nuclear medicine. Special thanks also to Mika Teräs, Ph.D., and Jarmo Teuho, M.Sc. (Tech), in Turku as well as to Stephan Nekolla, Ph.D., and Sebastian Fürst, M.Sc. (Tech), in Munich for welcoming me warmly to their institutions and for sharing their expertise in PET.

I express my gratitude to Professor Jari Hyttinen, Ph.D., Pasi Kauppinen, Ph.D., and Ville-Pekka Seppä, M.Sc (Tech), at the Tampere University of Technology for sharing their research

equipment with us in the two first studies of this thesis. Ville-Pekka is especially acknowledged for the valuable advice in bioimpedance measurements.

I am very grateful for all the support and expertise of the people at the Department of Applied Physics, University of Eastern Finland; the Department of Clinical Physiology, Nuclear Medicine and Clinical Neurophysiology, Kuopio University Hospital; Turku PET Centre, Turku University Hospital and Departent of Nuclear Medicine, Technische Universität München. Petro Julkunen, Ph.D., and Pekka Tiihonen, Ph.D., are especially acknowledged. I will also be forever grateful to Team 00: Heikki, Elisa, Alisa, Salla, Laura, Hanna, Matti, Timo, Helena and Minna; you made the days underground such fun.

I want to thank all my dear friends who have always been there for me, bringing joy into my life.

Finally, I want to thank my beloved parents, Raija and Seppo, for their love and support through my whole life.

My dearest thanks go to Eveliina for her love and support. During this thesis work, you have kept me firmly attached to real life outside the world of science by reminding me of the important things in life, such as travelling and cleaning the house.

This thesis work was financially supported by the Academy of Finland (International Doctoral Programme in Biomedical Engineering and Medical Physics as well as the Finnish Centre of Excellence in Inverse Problems Research, grant 250215), Kuopio University Hospital (EVO grant 5031345), Instrumentarium Science Foundation, Kuopio University Hospital Research Foundation, the Finnish Society of Nuclear Medicine, the Paavo Nurmi Foundation, the Foundation for Advanced Technology of Eastern Finland, Oskar Öflunds Stiftelse, and the North Savo Regional Fund of the Finnish Cultural Foundation.

Kuopio September 23, 2014

Tuomas Koivumäki

LIST OF ABBREVIATIONS

1D	One-dimensional
2D	Two-dimensional
3D	Three-dimensional
4D	Four-dimensional
AC	Attenuation correction
A-CTAC	Averaged computed tomography-based attenuation correction map
AMP	Amplitude-based cycle-wise respiratory gating
BIO	Bioimpedance-based gating
BMI	Body mass index
CEM	Complete electrode model
CT	Computed tomography
CTAC	CT attenuation correction
CWM	Chest wall motion
DE	Detector element
DIBH	Deep-inspiration breath-hold
DISP AP	Anterior-posterior displacement determined from the centre of the lesion
DISP CC	Cranial-caudal displacement determined from the centre of the lesion
ECG	Electrocardiography
EIT	Electrical impedance tomography
FDG	^{18}F-flourodeoxyglocose
FDOPA	Flourodihydroxyphenylalanine
FEM	Finite element method
FWHM	Full-width half-maximum
G-CTAC	Gated computed tomography-based attenuation correction map
GSO	Gadolinium oxyorthosilicate
ICG	Impedance cardiography
LM	List-mode
LOR	Line of response
LSO	Lutetium oxyorthosilicate
LYSO	Lutetium yttrium oxyorthosilicate

LVV	Left ventricular volume
MWT	Myocardial wall thickness
OSEM	Ordered subsets expectation maximization
PET	Positron emission tomography
PHA	Pulse height analyser
PMT	Photomultiplier tube
PNT	Pneumotachograph
PSF	Point spread function
PVE	Partial volume effect
RGT	GE Research Gating Tool
RPM	Real-time Position Management system by Varian Medical Systems
SNR	Signal-to-noise ratio
SPECT	Single-photon emission computed tomography
SUV	Standardized uptake value
SUV_{max}	Maximum standardized uptake value
SUV_{peak}	Peak standardized uptake value
SUV_{vol}	Volume which is delineated according to standardized uptake value threshold
TBR	Target-to-background ratio
TIME	Time-based cycle-wise respiratory gating
TOF	Time-of-flight

LIST OF SYMBOLS

c	Speed of light
D_0	Estimated overall displacement of the myocardium
D_{AP}	Anterior-posterior myocardial wall displacement
D_{CC}	Cranial-caudal myocardial wall displacement
D_{LAT}	Lateral myocardial wall displacement
d	PET detector ring diameter
E	Energy
e_l	l'th electrode
f	Frequency
I	Electrical current
I_l	Injected current on the l'th electrode
i	Imaginary unit, $i = \sqrt{-1}$
m	Mass
m_e	Electron mass
m_p	Positron mass
L	Number of electrodes
R_{in}	Intrinsic detector resolution
R_{nc}	Detector blur by noncolinearity
R_{pos}	Positron range, root mean square
R_{sys}	PET system resolution
S	Measurement sensitivity
s	Boundary of the electrode
U	Voltage
U_l^k	Voltage between measurement electrode pair k using current injection electrode pair l
U_l	Measured potential on l'th electrode
u	Electrical potential distribution
u_k	Potential distribution of electrode pair k, when it is used for current injection
v	Outward unit normal
x	Arbitrary point in volume conductor

Z	Impedance
z_l	Effective contact impedance on l'th electrode
ΔZ	Impedance change
ε_0	Permittivity of free space
ε_r	Relative permittivity
μ	Effective linear attenuation coefficient
σ	Conductivity
σ'	Admittivity
Ω	Volume conductor
ω	Angular frequency

LIST OF ORIGINAL PUBLICATIONS

This thesis is based on data presented in the following articles, referred to by the Roman numerals **I-IV**. The thesis also contains previously unpublished data.

I T. Koivumäki, M. Vauhkonen, J.T. Kuikka and M. A. Hakulinen "Optimizing bioimpedance measurement configuration for dual-gated nuclear medicine imaging: a sensitivity study," *Medical & Biological Engineering & Computing* **49**, 783-791 (2011).

II T. Koivumäki, M. Vauhkonen, J. T. Kuikka and M. A. Hakulinen "Bioimpedance-based measurement method for simultaneous acquisition of respiratory and cardiac gating signals," *Physiological Measurement* **33**, 1323-1334 (2012).

III T. Koivumäki, J. Teuho, M. Teräs, M. Vauhkonen and M. A. Hakulinen "Novel respiratory gating method for oncologic positron emission tomography based on bioimpedance approach," Submitted for publication.

IV T. Koivumäki, S. G. Nekolla, S. Fürst, S. Loher, M. Vauhkonen, M. Schwaiger and M. A. Hakulinen "Integrated bioimpedance – ECG gating technique for respiratory and cardiac motion compensation in cardiac PET," *Physics in Medicine and Biology*, In press.

AUTHOR'S CONTRIBUTION

Publications which are part of this thesis are original research papers. The author designed all the studies in collaboration with the co-authors. In study **I**, the author constructed the thorax model and performed all the computational analyses. In studies **I-IV**, the author performed all volunteer and patient measurements together with the co-authors, except for four measurements in study **III** (performed by J. Teuho) and one measurement in study **IV** (performed by S. Loher and colleagues). The author was mainly responsible for the data processing and analyses. However, in study **III**, J. Teuho performed image reconstructions with the RGT software and measured SUV_{peak} values. The data analysis scripts were developed by the author, except for the computational sensitivity analysis script of study **I** (by M. Vauhkonen and colleagues). The author of this thesis is the principal author of all these publications.

Contents

1 INTRODUCTION 17

2 POSITRON EMISSION TOMOGRAPHY 21
2.1 Principles of PET 21
2.2 Physical characteristics of PET 24
2.3 Attenuation correction 27
2.4 Reconstruction of PET data 29
2.5 Motion artefacts in PET 31
2.6 Motion compensation in PET 34
2.6.1 Cardiac gating 34
2.6.2 Respiratory gating methods 36
2.6.3 Motion correction methods 40
2.6.4 Breath-hold methods 41

3 BIOIMPEDANCE 43
3.1 Electrical properties of tissues 43
3.2 Bioimpedance measurement 44
3.3 Bioimpedance applications 48

4 AIMS OF THE PRESENT STUDY 51

5 MATERIALS AND METHODS 53
5.1 Measurement sensitivity optimization 53
5.2 Subjects 54
5.3 Physiological signal measurements 56
5.4 Clinical PET studies 58
5.5 Data analysis 61
5.5.1 Signal analysis 61
5.5.2 Image analysis 64
5.6 Statistical analysis 66

6 RESULTS 67
6.1 The optimized bioimpedance configuration 67
6.2 Validation of the measurement configuration 69
6.3 Bioimpedance-based respiratory gating in oncologic PET 73
6.4 Combined bioimpedance-based respiratory and ECG-based cardiac gating in cardiac PET 77

7 DISCUSSION 81
7.1 Determination and validation of the optimized bioimpedance measurement configuration 81
7.2 Evaluation of bioimpedance-based techniques in respiratory and dual gating of PET 84
7.3 Technical and future aspects of bioimpedance gating 87

8 SUMMARY AND CONCLUSIONS 93

REFERENCES 95

1 Introduction

Positron emission tomography (PET) imaging is susceptible to respiratory and cardiac motion artefacts due to the long image acquisition time. Respiratory and cardiac motion leads to image blur, which may distract qualitative image interpretation [55, 89, 91, 105, 121, 140] or distort the measurement of quantitative parameters, such as standardized uptake values (SUV) in oncologic imaging [89, 105]. As SUV parameters, for example, can be used in cancer staging and treatment response evaluation [105, 138, 156], the misinterpretation of images or quantitative parameters may, at worst, lead to misguided diagnosis, resulting in inadequate or unnecessary treatment.

The significance of motion artefacts and their minimization in PET are widely recognized. Cardiac motion is conventionally compensated utilizing gating based on electrocardiography (ECG) measurement. Respiratory motion compensation methods are based on three techniques. Gating is the sorting of reconstructable PET data according to the respiratory phase using direct or surrogate measurement of respiration [22, 24, 38, 46, 61, 73, 76, 89, 91, 105, 124, 125, 143, 158]. Motion correction techniques utilise motion data in the image reconstruction [20, 26, 49, 55, 67, 84, 85]. Specialized imaging techniques are based on breath-holding [71, 98, 99, 102, 107, 142, 160].

Despite extensive research, respiratory motion compensation methods have only been adopted slowly in clinical routine. Criticism has been expressed, for example, about the inadequacy of chest wall motion-based gating methods to follow lung motion [79] and inconsistency in gating [45]. On the other hand, direct airway measurements have been criticized for low patient tolerability [106]. In addition, data-driven methods may depend on radiopharmaceutical uptake, patient body habitus, or scanner geometry [29]. Further, there

are still relatively few clinical studies on motion correction methods with patient data, and breath-hold methods require good co-operation with the patient. Importantly, when simultaneous gating of respiration and cardiac function, that is dual gating, is pursued, the above-mentioned methods require a separate ECG system to enable versatile inclusion of cardiac gating.

Transthoracic bioimpedance techniques can be utilized in the evaluation of respiration [10, 48, 64, 93, 126, 129] and cardiac contractions [6, 23, 83, 113, 114]. Respiratory bioimpedance measurements reflect the change of thorax air content and shape as well as internal organ motion due to respiration [10]. They are used, for example, for apnoea detection as well as monitoring of intrathoracic fluid accumulations, such as lung oedema [10, 52, 128, 163]. Cardiac bioimpedance measurements, on the other hand, have been used to study the varying impedance due to changes in thoracic blood volume and flow [113], which are caused by cardiac contractions. Cardiac bioimpedance measurements are used for non-invasive detection of stroke volume, cardiac contractility, diastolic dysfunction, arrhythmias and systolic time intervals [13, 23, 81, 83, 113]. Importantly, when using bioimpedance methods, both respiratory and cardiac measurements can be conducted from the same measurement configuration using four standard ECG electrodes.

In spite of the potential feasibility of bioimpedance measurements for gating, only a few studies exist on the utilization of the bioimpedance technique in medical imaging: Cho et al. [33] and Conwell et al. [35] studied bioimpedance-based respiratory gating in myocardial perfusion single-photon emission computed tomography (SPECT) imaging. However, Cho et al. studied the method with healthy male volunteers and Conwell et al. imaged patients in the upright sitting posture, both of which are unusual for typical nuclear medicine studies. In addition, preliminary studies have been conducted on bioimpedance-based respiratory gating in other imaging modalities [101, 115].

The aim of the present thesis was to evaluate the feasibility of bioimpedance measurements for respiratory and cardiac motion compensation of PET imaging. First, an optimized electrode configuration was determined according to computational measurement sensitivity analysis (study **I**) and validated against the reference methods of pneumotachograph volume spirometry and ECG in volunteer measurements (study **II**). Bioimpedance respiratory gating was evaluated in oncologic PET imaging (study **III**). Further, integrated bioimpedance respiratory gating and ECG cardiac gating was evaluated in dual-gated cardiac PET (study **IV**).

2 Positron emission tomography

Positron emission tomography (PET) is a physiological imaging modality, which can be utilized to obtain clinically necessary diagnostic information based on tissue metabolism. The principle of PET was introduced in the 1950's, but wider clinical use started in the 1990's [119]. The benefits of PET, such as quantitative image information, and the intensive development of scanners, e.g. in terms of spatial resolution, have led to continuing growth in the demand for PET studies. Hybrid imaging systems, which enable the fusion of PET images with computed tomography (CT) or magnetic resonance (MRI) images that contain high resolution anatomical information, offer valuable tools in accurate anatomical localization of functional PET results. PET is widely used in oncologic, cardiac and neurologic imaging.

2.1 PRINCIPLES OF PET

Nuclear medicine imaging is based on the detection of emission photons produced by a radiopharmaceutical. Radiopharmaceuticals consist of radioactive nuclides and biological substrate molecules. PET radionuclides are positron emitters, which typically have short half-lives; thus they often require on-site production in the form of a cyclotron or disposable generator (Table 2.1). Biological substrates take part in natural metabolic processes and thus determine radiopharmaceutical distribution in the body. ^{18}F-Fluorodeoxyglucose (^{18}F-FDG or FDG for short) is the most commonly used PET radiopharmaceutical (Table 2.1), largely due to the relatively long half-life of ^{18}F, which allows the use of FDG outside cyclotron sites. FDG is

metabolized similarly to glucose, but its metabolite (FDG-6-phosphate) [36] remains trapped within the cell. As the concentration of the metabolite in the cell grows in proportion to the glucose metabolic rate of the cell, FDG uptakes represent the extent and distribution of glucose metabolism in the tissue [157]. FDG studies are used, for example, in oncology to highlight tumours with increased glucose metabolism; in cardiology they are used to study the viability or inflammatory activity of the myocardium [15, 157, 161].

Table 2.1: *Typical PET radionuclides with related half-lives ($T_{1/2}$), maximum kinetic energy (E_{max}) and positron range (R_{pos}) as well as examples of radiopharmaceuticals [16, 51, 133, 150, 159, 162].*

Radionuclide/ Radiopharmaceutical	**$T_{1/2}$ [min]**	**E_{max} [MeV]**	**R_{pos} [mm]**	**Target of application**
Cyclotron-produced				
^{11}C	20.4	0.96	4.1	
^{11}C-methionine				Brain and prostate cancer
^{13}N	9.98	1.19	5.4	
^{13}N-ammonia				Myocardial perfusion and blood flow
^{15}O	2.03	1.70	8.0	
^{15}O-water				Myocardial perfusion and blood flow
^{18}F	110	0.69	2.4	
^{18}F-fluorodeoxyglucose				Tumour targeting, myocardial viability, cerebral glucose metabolism, infection and inflammation
Generator-produced				
^{68}Ga	68.0	1.90	9.0	
^{68}Ga-DOTA-conjugates				Somatostatin receptor imaging, neuroendocrine tumours
^{82}Rb	1.25	3.36	17	
^{82}Rb-chloride				Myocardial perfusion and viability

PET imaging is based on the detection of annihilation events, which originate from a radiopharmaceutical typically administered by an intravenous injection. Annihilation follows as the positron, emitted by the neutron-deficient radionuclide as a consequence of β^+ decay, dissipates most of its kinetic energy in tissue interactions and finally annihilates itself in an incidence with an electron [116]. Due to annihilation, positron and electron mass, m_e and m_p, are converted into electromagnetic energy E according to mass-energy equivalence

$$E = mc^2 = m_e c^2 + m_p c^2, \tag{2.1}$$

where c is the speed of light. The result is two 511 keV photons emitted in opposite directions due to the conservation of momentum.

Annihilation photons are detected by the detector ring in the PET system (Figure 2.1). After a valid detection of a coincidence event, the location of annihilation can be estimated on a line, or more precisely a volume, between photon detectors, that is, the line of response (LOR) [119]. For PET image formation, acquisition and reconstruction of LOR data from multiple angles and radial offsets of the imaged object are required.

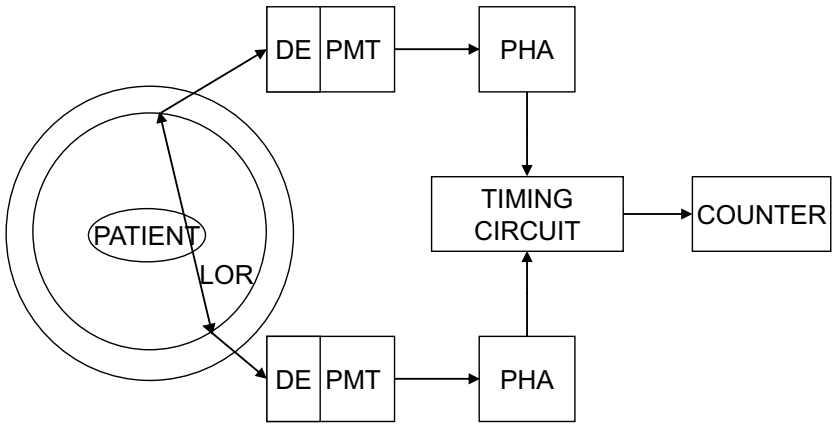

Figure 2.1: *Annihilation photons are conventionally absorbed into detector elements (DEs), transformed into electrical signal, and amplified by photomultiplier tubes (PMTs). In the most recent systems, the electrical signal is produced by semiconductor detectors. Scattered photons are rejected in pulse height analysers (PHA), which discriminate photon energies outside an accepted range of, for example, 350-650 keV [116]. Valid coincidences, whose annihilation photons are detected in the timing circuit within a 5-12 ms coincidence time window [119], are recorded for each line of response (LOR) by the counter [116]. Figure modified from [116].*

2.2 PHYSICAL CHARACTERISTICS OF PET

The validity of LOR evaluation is inherently reduced by noncolinearity, positron range and parallax error, or depth-of-interaction effect, all of which contribute to the characteristic blur of PET images. Noncolinearity follows from the conservation of momentum. The positron may still possess kinetic energy at the instant of annihilation; thus, the annihilation photons may depart up to 0.5° from the expected 180° angle (Figure 2.2A) [116, 119]. Noncolinearity causes an image blur R_{nc} related to the diameter d of the detector ring

$$R_{nc} = 0.0022d. \qquad (2.2)$$

Root-mean-square positron range R_{pos} , that is the linear distance travelled by the positron before annihilation, depends on the initial kinetic energy of the positron. The maximum positron range in water varies between 2.4 and 17 mm with the most common radionuclides (Figure 2.2A) (Table 2.1). LOR can also be mispositioned due to parallax error, which may occur if the photon arrives at the detector at an oblique angle. The photon may then be absorbed in the adjacent detector and not the one it arrived at, leading to incorrect determination of the LOR (Figure 2.2B) [87]. Parallax error is strongest in the periphery of the detector ring.

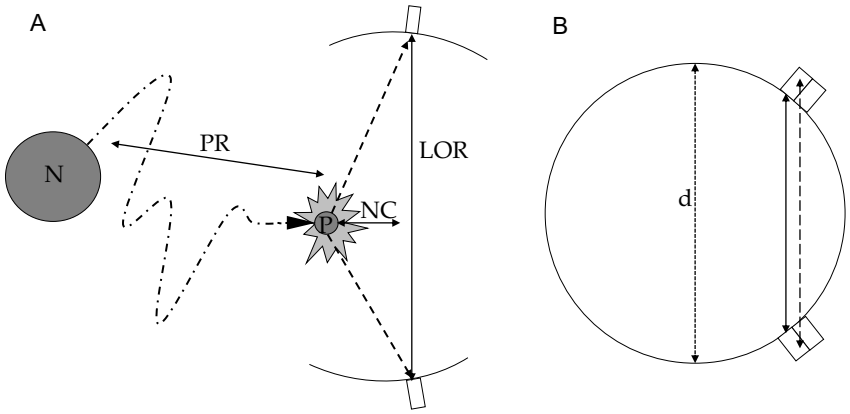

Figure 2.2: *In A, positron P is emitted from the neutron-deficient nucleus N. Detected coincidence photons are connected by the line of response, LOR. The distance travelled by the positron before annihilation (positron range, R_{pos}) and the noncolinear (NC) deviation determine limits for the inherent spatial resolution of the PET. In B, LOR is defined incorrectly (solid arrow) due to parallax error, which follows from photon penetration to adjacent detector elements (dashed arrow). Figure modified from [116].*

The size of the detector crystal determines the intrinsic spatial resolution of the detector R_{in} , which is often quantified determining the full-width half-maximum (FWHM) of the point spread function (PSF). PSF is the position spectrum of a point source in a fixed distance from the detector [87]. PSF is skewed on the edge of the detector ring by the parallax effect [116]. Finally, PET system resolution R_{sys} is determined as

$$R_{sys} = \sqrt{R_{in}^2 + R_{nc}^2 + R_{pos}^2}. \quad (2.3)$$

Modern PET systems have been reported to have spatial resolutions of 4.4-5.9 mm when measured using standardized NEMA NU 2-2007 protocol and ^{18}F [17, 68, 103].

The essential information in PET acquisition consists of true events, that is, coincidence events that originate from the same annihilation (Figure 2.3A). Single events (Figure 2.3B), on the other hand, may increase system dead time leading to pulse pile-up and loss of events. These, in turn, result in radiopharmaceutical uptake underestimation at high counting rates. Dead time losses are minimized by correction models based on the observed count rates of different radiopharmaceutical concentrations [32]. In case a true event is detected temporally close to a single event or another true event, such multiple coincidence detection leads to rejection of detected events [116].

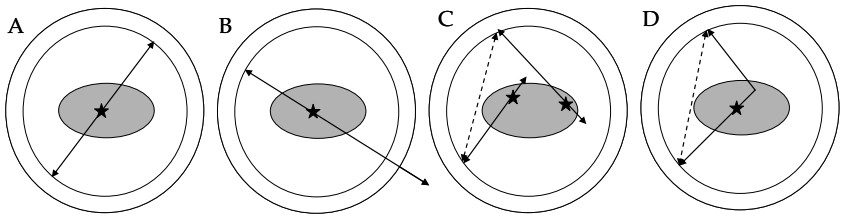

Figure 2.3: *True coincidence (A), single (B), random (C) and scattered (D) events. In single events, the other photon is directed out of the detector circle or has an energy too low for detection. In random events, the detection is related to different annihilations. With scattered events, the detection is based on the same annihilation but is falsely positioned due to Compton scattering. Figure modified from [116].*

Random (Figure 2.3C) and scattered (Figure 2.3D) events produce undesired background noise in PET images; they reduce contrast and are detrimental to quantification as they are not related to real radiopharmaceutical accumulation [116]. Random events can be corrected to some extent from the PET data by statistical estimation according to element-wise singles

rate detection in the PET system or by using a delay circuit in coincidence detection [116]. Scatter correction is done by using models that are based either on a function fitting to events that have been detected outside known activity distributions, scatter window subtraction, or 3D scatter modelling of uncorrected PET data [116].

In addition to dead time, random event and scattered event corrections, the photon detection efficiency of all detector block pairs, that is LORs, in the PET system has to be uniform. Detector nonuniformity, caused by differences in physical dimensions, geometry and electronics of detectors, is corrected by normalization using a uniform plane or cylinder source and deriving normalization correction factors for each detector pair or detector of the system [116].

PET data corrections are typically included in the image reconstruction. The development of fast detector materials, e.g. lutetium oxyorthosilicate (LSO), lutetium yttrium oxyorthosilicate (LYSO) as well as gadolinium oxyorthosilicate (GSO), and electronic circuits has improved the time resolution of photon detection and enabled estimation of the annihilation location on the LOR. This time-of-light (TOF) method is based on the time difference between the two annihilation photon detections. In addition, PSF correction, which is used to improve spatial image resolution especially on the periphery of the image where the PSF is most skewed and broad, can be incorporated in the reconstruction algorithms.

2.3 ATTENUATION CORRECTION

Annihilation photons are prone to interact with tissue while traversing it. The interaction mostly occurs through Compton scattering leading to change in photon direction and decrease of photon energy [116]. Thus, some photons are not detected, or they are attenuated. The effect of photon attenuation can be seen as pronounced radiopharmaceutical uptake on the surface of the imaged object, whereas uptake deeper in the object is

suppressed (Figure 2.4) [116]. Attenuation correction (AC) is used to account for the unequal attenuation properties in different parts of the imaged object.

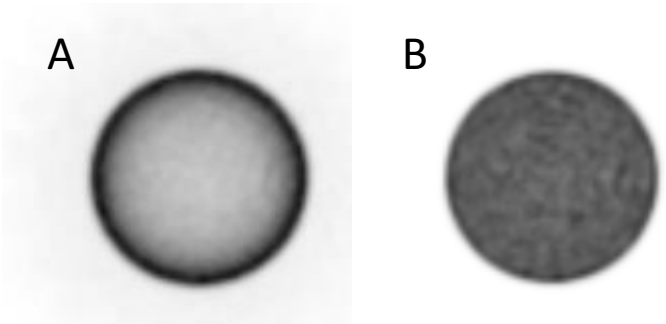

Figure 2.4: *Homogeneous quality control phantom image without (A) and with (B) attenuation correction.*

Attenuation correction (AC) can be performed computationally assuming constant attenuation throughout a homogenous object. This approach is sometimes used for phantom or brain studies [116]. However, if the imaged object is more heterogeneous, as the human thorax for example, more accurate estimation of photon attenuation is needed. Photon attenuation can be measured performing a transmission scan using either external ring or rod sources, e.g. of ^{68}Ge, or CT acquisition [116, 155]. At present, CT is preferred due to the speed and the capability of producing high-resolution attenuation maps with nearly no statistical uncertainty [155].

A CT image is based on the detected attenuation of X-rays that traverse the patient. In CT acquisition, an X-ray tube rotates around the patient transmitting X-rays, which are detected on the opposite side of the gantry. The CT image represents the pixel-wise effective linear attenuation coefficients, μ, throughout the imaged volume. However, attenuation coefficients acquired with the continuous energy spectrum of CT have to be scaled to 511 keV to derive attenuation correction estimation for PET acquisition (Figure 2.5) [155].

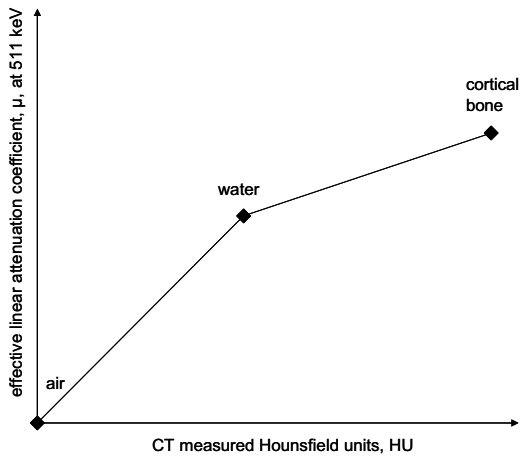

Figure 2.5: *Bilinear conversion model from CT-derived linear attenuation coefficients, presented in Hounsfield units, to attenuation coefficients at 511 keV. The slope of the air-water section is not sensitive to CT acquisition voltage whereas the slope of the water-bone part depends on CT voltage. Figure modified from [155].*

As the MRI scan in PET/MR systems does not provide direct information on attenuation, the attenuation correction map in these systems has been initially determined based on specific MR sequences and subsequent segmentation of, for example, 2-5 tissues with designated linear attenuation coefficients [37, 72, 95, 151]. In addition, other approaches, such as atlas and machine learning as well as PET emission data-based methods, are being actively investigated [41, 62, 104]. However, it has been reported that MR-based attenuation correction may lead to substantial and region-dependent underestimation of quantitative PET values [7, 44, 72].

2.4 RECONSTRUCTION OF PET DATA

Modern PET scanners utilize 3D acquisition; that is, although the detector ring consists of multiple element rows, photon detection is possible with all detector element combinations [116]. The prerequisite for 3D acquisition is LOR-based electronic collimation, which is characteristic for PET, as opposed to absorptive collimators used in other nuclear

medicine instruments [116]. The advantage of 3D acquisition is the high sensitivity, which enables a high signal-to-noise ratio (SNR), short imaging times and small injected patient doses [116].

The acquired PET data is typically stored in the histogram mode as the number of events detected in each LOR. On the other hand, list-mode (LM) acquisition can be used to collect information on the detection location and the time of the detection of the annihilation photons; this enables flexible post-processing of the data [116].

Regardless of the format, data is transformed into sinograms prior to image reconstruction. Basically, sinograms are 2D representations of the data in matrix form, where rows illustrate the radionuclide accumulation of the object in all projections and columns represent its radial distance from the image centre [116]. Similar representations can also be found for 3D cases [40].

Analytic reconstruction methods, most importantly filtered backprojection (FBP), are conventional in medical imaging. However, FBP has some drawbacks such as inaccurate modelling of PET detector geometry, leading to nonuniform sensitivity [116]. FBP neither accounts for positron range nor noncolinearity [116]. Further, FBP assumes noise-free data and weighs all LORs equally; this may result in streak artefacts, as the assumption rarely holds for PET data [116].

Iterative image reconstruction, as an alternative to analytic methods, is performed in repeated cycles. The reconstruction begins with an initial guess of the image. Second, projection profiles of the initial guess image can be computed using simple forward projection algorithms. However, sophisticated approaches include modelling of PET system properties, such as noncolinearity, detector characteristics and positron range, to the profile computation step, enabling higher quantitative accuracy and spatial resolution [116]. The computed projection profiles are compared to the measured ones and adjusted to minimize their mutual difference. This adjustment is done under the conditions of maximum likelihood

or expectation maximization methods, for example, to minimize or maximize the related cost function. Similar comparison and adjustment cycles, iterations, are conducted until the required match with the measured activity distribution is achieved. Computationally intensive iterative methods are typically more time-consuming than analytic methods. However, they can be sped up by dividing the projection angles into smaller groups and by conducting parallel calculations using, for example, ordered subsets expectation maximization (OS-EM) algorithms. Iterative reconstruction methods are able to produce higher spatial resolution and signal-to-noise ratio than backprojection images; this is due to better statistics and system modelling [116].

2.5 MOTION ARTEFACTS IN PET

A standard static PET image acquisition typically requires at least 90 seconds per bed position. The long imaging time predisposes image acquisition to motion that originates from patient respiration and cardiac function as well as in some cases from patient movement. The movement of the whole patient is rare and minimized by fixation and ensuring patient comfortability. In case significant whole patient movement is observed, the image acquisition is typically repeated.

Respiratory and cardiac motion is inevitable during the imaging procedure. The mean respiratory motion of lung and liver lesions as well as the heart is largest in the cranial-caudal direction and smaller in lateral and anterior-posterior directions (Table 2.2). Cardiac contraction itself has been reported to cause an approximately 8-10 mm cranial-caudal and 8-24 mm lateral cycle-wise shift in the myocardium [154]. Further, when there are oncologic lesions in the proximity of the myocardium, their motion has been estimated to reach 4 mm due to cardiac contractions [130]. Additionally, even a 5 mm hysteresis, that is, a different transition path of lesion in inspiration and expiration, may occur in respiratory motion [130]. All these motions are

noteworthy when compared to the 4.4-5.9 mm spatial resolution of modern scanners [17, 68].

Table 2.2: *Overview of respiratory motion extents of lesions and the myocardium. The motion extent is expressed as mean ± standard deviation.*

Observer	Subject	Modality	Motion extent
Seppenwoolde et al. [130]	Lung tumours	Fluoroscopy	CC: 12 ± 2 mm AP: 2.2 ± 1.9 mm LAT: 1.2 ± 0.9 mm
Kitamura et al. [75]	Liver tumours	Fluoroscopy	CC: 9 ± 5 mm AP: 5 ± 3 mm LAT: 4 ± 4 mm
Plathow et al. [117]	Lung tumours, lowest third of the lungs	MRI	CC: 9.5 ± 4.9 mm AP: 6.0 ± 2.8 mm LAT: 6.1 ± 3.3 mm
Schechter et al. [132]	Heart	Biplane angiography	CC: 4.9 ± 1.9 mm AP: 1.3 ± 1.8 mm LAT: 0.4 ± 2.0 mm
Livieratos et al. [91]	Centroid of cardiac blood pool	PET	CC: 8.5 ± 4.8 mm AP: 2.4 ± 0.9 mm LAT: 2.5 ± 2.2 mm
Martinez-Möller et al. [96]	Inferior myocardial wall	PET	CC: 5.5 ± 2.2 mm 3D: 5.8 ± 2.2 mm

MRI: magnetic resonance imaging, PET: positron emission tomography, CC: cranial-caudal, AP: anterior-posterior, LAT: lateral, 3D: three-dimensional motion.

Respiratory motion is a significant error source in oncologic PET imaging. Motion leads to image blurring and thus to reduced image quality (Figure 2.6) [89, 105]. The effect is similar to the partial volume effect (PVE), which arises from the limited spatial resolution and pixel-wise image representation of the PET system, both of which lead to image blurring [135]. In general, small lesions are more sensitive to respiratory motion artefacts than large ones [89]. Further, large motion amplitudes as well as highly varying respiratory patterns emphasize artefacts and the proximity to the diaphragm increases the effect of motion [89].

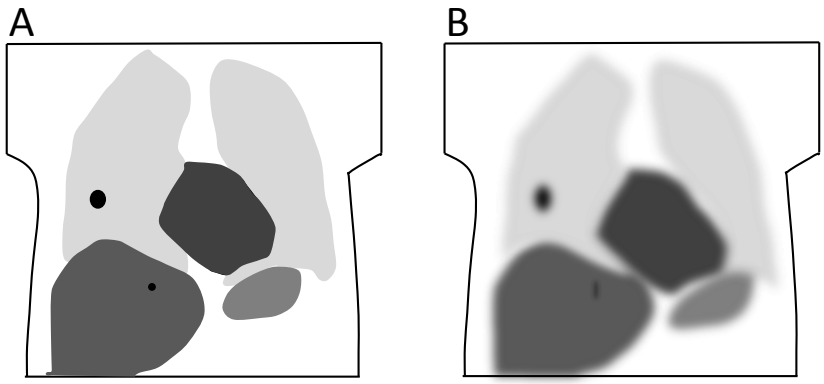

Figure 2.6: *Schematic image of the thorax with lung and liver lesions without (A) and with (B) motion. Lesions (black) are evidently blurred in B, and the visibility of the small liver lesion is compromised. The figure is created using image processing and is based on arbitrary motion. Figure modified from [89].*

In addition to its effect on the qualitative, visual interpretation of lesions, motion may distort quantitative evaluation, which in oncologic FDG studies is often based on the semi-quantitative standardized uptake value (SUV) and the diameter or volume of the lesion [105]. SUV is determined as the ratio of activity concentration measured in a voxel and injected dose [119]. In addition, the ratio is normalized using either the body mass, lean body mass or body surface area of the patient; of these, the use of lean body mass has been recommended [153]. Motion may lead to the underestimation of SUV and overestimation of volume [105]. Variance in SUV measurements may jeopardize the reliability of PET follow-up studies as SUV is widely used for cancer staging and treatment response evaluation [105, 138, 156]. Similarly to oncologic imaging, motion blur distorts cardiac PET imaging. Physiological motion may hinder the detection of coronary plaques [140] and degrade the quality of myocardial images [91] as well as the quantification of myocardial uptake estimates [121].

Together with motion during PET data acquisition, the coregistration of PET data and the CT attenuation correction (CTAC) map is important. PET data is recorded over many cycles of respiration and cardiac function. However, a standard

CTAC scan captures only an instant of the respiratory and cardiac state. Thus, PET and CT image fusion accuracy may be poor and lead to a mismatched attenuation map [47, 74, 112]. Mismatched attenuation map may pose attenuation correction artefacts such as the under- or overestimation of SUV [89]. In contrast to standard CTAC, a more reliable attenuation correction may be achieved using a four-dimensional CT scan (4D CT), which records CT data continuously during the respiratory cycle. The 4D CT can be used to reconstruct an averaged attenuation map over the whole respiratory cycle [74, 89, 112]. The most accurate attenuation correction can often be achieved when gated 4D CT, which is phase-matched with the gated PET image, is used for the generation of the attenuation map [74]. The drawback of 4D CT, however, is that it cannot be used on all patients due to a higher radiation burden compared to the standard clinical low-dose attenuation correction CT.

2.6 MOTION COMPENSATION IN PET

The significance of motion artefacts and their minimization in PET/CT are widely recognized. The importance of motion correction keeps growing as the spatial resolution of imaging systems evolves and images become more prone to motion artefacts. In addition, there is great demand for motion compensation, that is, the recovery of high spatial accuracy. This is due to the development of advanced radiotherapy techniques, such as intensity-modulated radiotherapy, which require precise target localization and enable treatment margin reductions [79].

2.6.1 Cardiac gating

Cardiac motion is universally taken into account using electrocardiographic (ECG) gating [27, 157]. ECG measures the electrophysiological function of the heart. The electrical activation of the heart originates in the sinus node. At first, the activation spreads to the atria, causing atrial contraction and filling of the ventricles. After a short delay in the

atrioventricular node, the activation propagates to the ventricles, leading to the contraction of the ventricles and the ejection of blood to systemic and pulmonary circulation. Importantly, the onset of ventricle contraction with the associated electrical depolarization can be seen as a QRS complex in the ECG signal (Figure 2.7A) [94]. The R wave of a QRS complex is commonly used as a timing trigger in medical imaging gating applications [27, 157]. In the medical imaging context, ECG is typically measured using the Mason-Likar modification of the limb leads measurement (Figure 2.7B) [97].

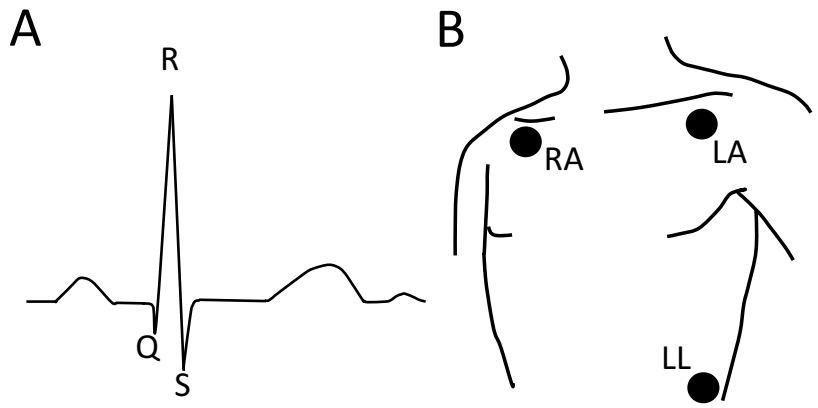

Figure 2.7: *(A) ECG cycle with marked QRS complex. (B) Mason-Likar ECG measurement configuration, where the right and left arm electrodes (RA and LA) and the left leg electrode (LL) are positioned on both infraclavicular fossa and left iliac crest [97]. Figure modified from [94].*

In ECG gating, cardiac cycles are divided into temporal bins according to the detected R waves (Figure 2.8). ECG-gated image data is formed by reconstructing an image of each mutually corresponding data bin and arranging these images in a series. This image series, though it suffers from reduced SNR due to data partition into bins, presents an averaged cardiac cycle and can be used for the determination of functional cardiac parameters, such as the ejection fraction.

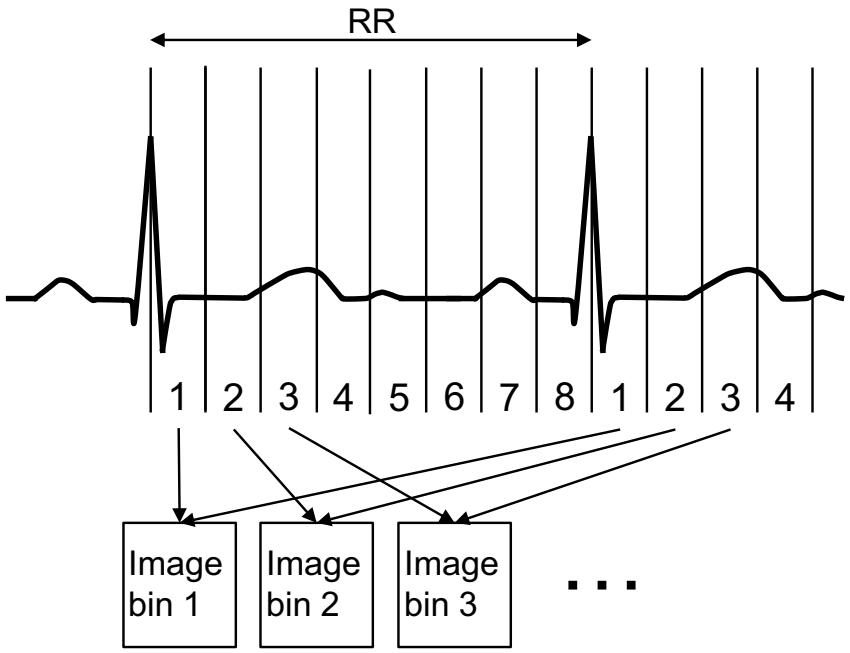

Figure 2.8: *Principle of cardiac gating. RR intervals are divided into mutually corresponding time bins, which are used to reconstruct images. Each image corresponds to a certain phase in the cardiac cycle.*

2.6.2 Respiratory gating methods

The approximate volume of normal respiration is 500 ml [59, 60]. However, total lung volume may vary in the range of 1000-6000 ml between residual volume and total lung capacity [59, 60]. Lung volume changes are linked with the motion of the thorax as the inward-outward motion of the ribs as well as the lengthening and shortening of the chest cavity due to diaphragm movement.

Respiratory volume can be determined by integrating an airflow measurement, which is commonly performed using a pneumotachograph (PNT) (Figure 2.9). PNTs are clinically accurate and have an approximately linear pressure-flow relationship [120]. The PNT element is typically heated to prevent the condensation of water vapour into the element as condensed water affects the flow resistance of the PNT [120].

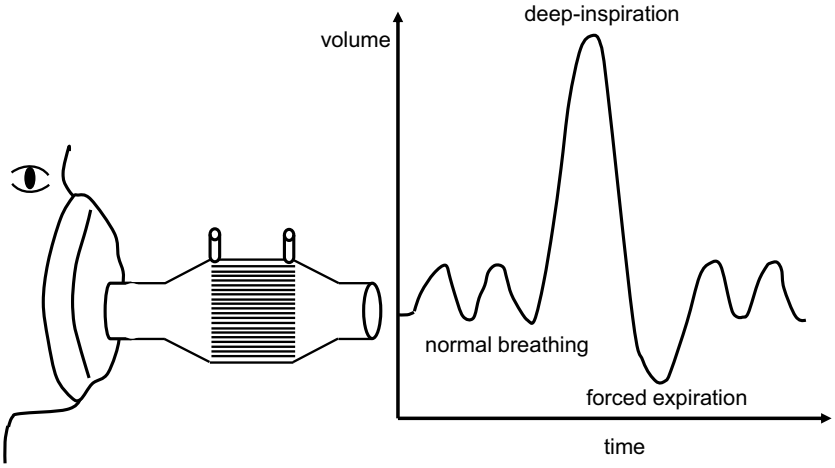

Figure 2.9: *The measurement of pressure difference is performed with a pneumotachograph and face mask. The flow output is integrated to obtain a volume curve.*

Respiratory gating is based on PET data sorting according to the respiratory phase, similarly to cardiac gating. Thus, the PET data of only mutually matching phases of respiration are used in the image reconstruction. The division can be made in time or amplitude and is conventionally performed in bins of equal duration or height [38] (Figure 2.10). However, in general, amplitude-based gating methods are preferred due to their robustness against variations in respiratory cycle length and depth [38, 139]. By division of the data into bins, the respiratory motion within a bin is essentially smaller than in the non-gated study thus enabling the reduction of motion blur and yielding a potentially more accurate definition of quantitative parameters. The drawback of gating is the decreased SNR, which follows from lower image statistics due to the omission and partition of the PET data. The decreased SNR of gating studies is typically compensated by extending image acquisition time. To optimize the relationship of small intra-bin motion and decreased SNR, specialized amplitude gating methods have been introduced. Such methods are typically based on histogramming the respiratory amplitude data and utilization of the part of the respiratory cycle which has the least motion, typically end-expiration [50, 90, 143]. This

approach potentially enables a high degree of data, and SNR, preservation with small intra-bin motion.

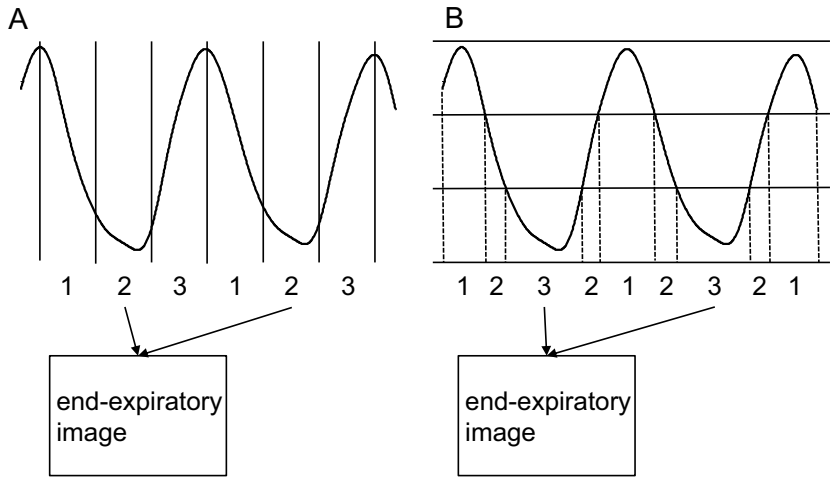

Figure 2.10: *Time- (A) and amplitude-based (B) respiratory gating. The figure illustrates how end-expiratory image data is gathered in typical respiratory gating approaches.*

Respiratory gating is often based on a surrogate respiration measurement of chest wall motion (CWM) by camera tracking or a measurement belt [24, 38, 76, 89, 91, 105]. Current commercial implementations, such as Real-time Position Management (RPM) by Varian Medical Systems (Palo Alto, CA, USA) and AZ-733V by Anzai Medical Co. (Tokyo, Japan), are based on CWM measurement (Figure 2.11). However, direct airflow measurement methods can also be used in respiratory gating [22, 46, 158]. Recently, methods that determine respiratory motion solely from the acquired PET data have been introduced. These are also referred to as data-driven methods and are based on centre-of-mass tracking, inhomogeneous sensitivity of the scanner or spectral analysis, for example [24, 28, 61, 73, 124, 125].

In addition to plain respiratory gating, dual gating methods, which integrate respiratory gating with cardiac gating, have been introduced [76, 80, 96, 140, 141]. Dual gating methods

are based on simultaneous acquisition of respiratory and cardiac gating signals and the division of the data into bins, considering both respiratory and cardiac phases. This results in images with minimized cardiac and respiratory motion. On the other hand, dual-gated images have a low SNR, as for example in the case of 8 cardiac bins and 3 respiratory bins, one dual gated bin may contain only 1/24 of the whole acquisition data.

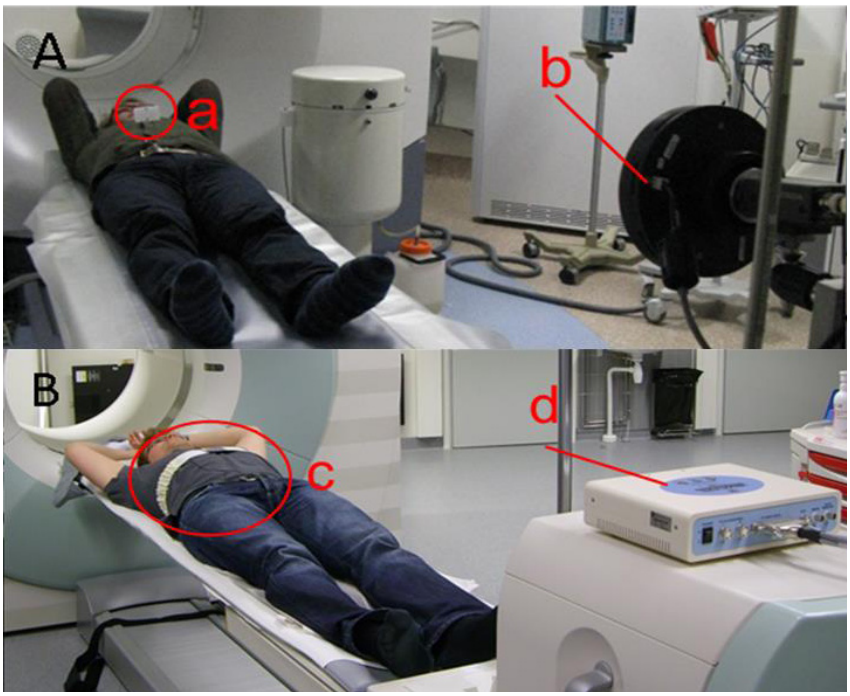

Figure 2.11: *RPM (A) and AZ-733V (B) gating devices. RPM tracks the motion of a box with reflective markers (a) on the patient's thorax by infrared camera (b). AZ-733V uses a pressure sensor belt (c) to measure chest wall motion (CWM). The motion signal is recorded by a wave deck (d).*

Despite the drawback of data omission and the resulting decreased SNR or lengthened acquisition times, at present gating methods are the most versatile and widely used means of respiratory artefact compensation. However, despite their availability, gating methods have entered clinical routine slowly. This may be related to the complicated and cumbersome use of these techniques.

Studies generally show a good relation between CWM and internal organ motion [14, 54, 63, 65]. However, some studies have reported that the measurement of a single external landmark may be an inaccurate surrogate for internal organ motion and have notable intersubject variability [63, 79]. In addition, current scanner controlling trigger implementations may suffer from inaccuracies and be incoherent between different manufacturers [45, 110]. Direct airflow measurements, on the other hand, may not be tolerated by patients in long acquisitions [106]. The most significant challenge with PET raw data-based data-driven gating methods is the performance dependency on the radiopharmaceutical uptake characteristics as well as on the patient habitus and scanner geometry [29].

2.6.3 Motion correction methods

In contrast to respiratory gating methods, which omit part of the data, the primary aim and advantage of motion correction methods is the utilization of all acquired PET data, thus maintaining a high SNR. The main idea of motion correction methods is to utilize motion information which is recorded or computed during the image acquisition in the reconstruction of a single motion-free image.

Image registration methods fuse gated images together using an optical flow algorithm [39, 77, 78] or regularization algorithms [8, 9]. Methods that are based on a time-varying system matrix use motion information from pre-reconstructed images during the final reconstruction [49, 85], whereas event rebinning methods utilize the information prior to reconstruction [26, 84]. Joint reconstruction methods incorporate motion estimation and image reconstruction [20, 55, 67].

Non-rigid motion correction methods (time-varying system matrix and joint-reconstruction) can generally be considered more versatile than rigid (rebinning) methods, especially when the whole image volume is to be corrected instead of a smaller volume of interest which contains single organs [85]. Alternatively, registration methods have been criticized for lower image quality [5, 85] although comparable

image quality between a registration and a joint reconstruction method has also been reported [5, 118]. So far, studies on motion correction methods have mostly been methodological with very few patients. None of the methods presented has established a foothold in clinical practice.

2.6.4 Breath-hold methods

In addition to PET data processing in terms of gating and motion correction, dedicated imaging techniques have been utilized to limit the PET data acquisition to a certain respiratory phase to avoid respiratory motion artefacts. In oncologic PET imaging, the inclusion of end-inspiratory CT in the imaging protocol has been recommended for the better detectability of small nodules [3]. Deep-inspiration breath-hold (DIBH) techniques have also been introduced in the field of PET [71, 98, 99, 102, 107, 142]. In addition, expiratory breath-hold has been suggested [160]. These breath-hold methods have been reported to improve quantification and coregistration between PET and CT. However, the breath-holding manoeuvre is not suitable for all patients as a high level of patient cooperation is required and even a 20-s breath-hold may be impossible with patients suffering from lung diseases, such as emphysema or pulmonary fibrosis [142].

3 Bioimpedance

3.1 ELECTRICAL PROPERTIES OF TISSUES

The electrical bioimpedance of a tissue determines the ability of the tissue to withstand electrical current. In the biomedical context, bioimpedance properties of tissues (Table 3.1) are typically described utilizing conductivity and permittivity

$$\sigma' = \sigma + i\omega\varepsilon_0\varepsilon_r = \sigma + i2\pi f\varepsilon_0\varepsilon_r, \tag{3.1}$$

where σ' is admittivity, the inverse of impedivity; σ conductivity, the inverse of resistivity; $i = \sqrt{-1}$ an imaginary unit; ω angular frequency at frequency f; ε_0 = 8.854187817·10^{-12} *F/m* permittivity of free space; and ε_r relative permittivity [58]. The resistive properties of tissues are defined by the intra- and extracellular media of cells, whereas dielectric properties are defined by capacitive cell membranes. However, often in bioimpedance applications, it is assumed that the electrical properties of tissues are dominated by resistivity. This approximation is valid when [108]

$$\frac{\omega\varepsilon_0\varepsilon_r}{\sigma} \ll 1. \tag{3.2}$$

However, according to Equation 3.2, neglecting capacitive effects is slightly controversial. For example, when the values for muscle and deflated lung given in Table 3.1 are used, the left side of the equation approximately equals 0.13. On the other hand, it has been stated that resistivity is the dominant component, even at a frequency as high as 10 MHz [58].

Table 3.1. *Tissue conductivities and relative permittivities at 100 kHz [4, 53].*

Tissue	**Conductivity [S/m], σ**	**Relative permittivity, ε_r**
Blood	0.70	5100
Cancellous bone	0.084	470
Fat	0.024	93
Myocardium	0.22	9800
Lung, deflated	0.27	5100
Lung, inflated	0.11	2600
Muscle	0.36	8100

Tissues are considered to be volume conductors that have continuous distribution of electrical properties. Due to anisotropy, the electrical properties may vary significantly in different directions. The human thorax can be modelled as a finite piece-wise homogenous volume conductor, in which organs are modelled as homogenous volume conductors [94]. Importantly, the electrical properties of the thorax vary in time due to changes in blood volume and flow following the cardiac cycle as well as the respired air following the respiratory state [6, 10, 11, 48, 56, 64, 81, 94, 113, 114, 129].

3.2 BIOIMPEDANCE MEASUREMENT

Bioimpedance measurement is based on Ohm's law

$$Z = \frac{U}{I}, \tag{3.3}$$

which defines impedance Z as the ratio of measured voltage U and the known injection current I. The current is typically in the milliamp range at a frequency of 20-100 kHz [94]. The current is never higher than 10 mA as defined in the EN 60601-1 standard. In conventional bioimpedance measurements, two electrodes are used for current injection. The voltage induced by the current can be measured utilizing the same two electrodes as for current injection (two-electrode method) or a separate pair of

electrodes (four-electrode method) [109]. However, different electrode pairs for current injection and voltage pick-up are preferred in order to achieve increased robustness for movement artefacts and distortions in contact impedance [10, 109, 123, 144].

Bioimpedance measurement is used to define the electrical impedance of a body part or tissue between the electrodes. The measurement sensitivity is highest near the electrode circumference and reaches deeper into the measured volume when the electrode distance is increased (Figure 3.1) [58]. However, also in the case of large electrode separation, relative sensitivity remains highest in the surface of the volume conductor near the electrodes [58].

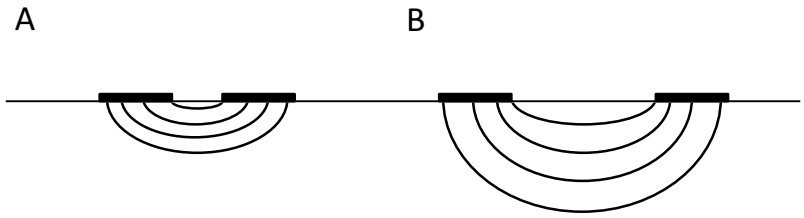

Figure 3.1: *Measurement sensitivity reaches deeper in the tissue in the case of a large electrode distance (B) compared to a small electrode distance (A). The solid lines between the black electrodes represent schematic isosensitivity lines. Figure modified from [58].*

In computational models, measurement sensitivity $S_n^{k,l}$ in the n'th element using a voltage measurement electrode pair k and a current injection pair l (Figure 3.2) can be computed in the discretized form as the susceptibility of observing a voltage change δU_l^k between measurement electrodes k, by the conductivity change $\delta\sigma_n$

$$S_n^{k,l} = \frac{\delta U_l^k}{\delta \sigma_n}. \tag{3.4}$$

In a larger volume of interest, such as the human body or certain organs, for example the heart or lungs, the sensitivity of

a measurement configuration can be determined as the sum of its element-wise sensitivities,

$$S^{k,l} = \sum_{n=1}^{N} S_n^{k,l}. \tag{3.5}$$

Interestingly, in terms of measurement sensitivity, the electrode locations of the current injection and voltage pick-up electrodes are interchangeable according to the reciprocity theorem of Helmholtz [94].

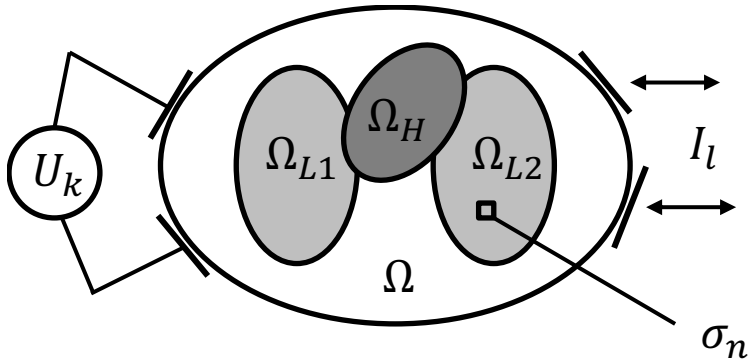

Figure 3.2: *Schematic representation of thoracic bioimpedance measurement. I_l illustrates current feed, U_k voltage measurement, σ_n conductivity of element n and Ω, Ω_{L1}, Ω_{L2} as well as Ω_H different volumes of interest in the volume conductor.*

The measurement sensitivity can be calculated, for example, by utilizing the complete electrode model (CEM) of electrical impedance tomography (EIT). There are also other electrode models for EIT, such as the continuum, gap and shunt models [144]. However, the continuum and gap models have been found to overestimate measured resistivities since they ignore the shunting effect of the electrodes and electrode contact impedances [30, 134, 144]. The shunt model takes into account the shunting effect, but as it still ignores electrode contact impedances, it has been reported to underestimate resistivities [134, 144]. CEM is very accurate as it considers both the effects of electrode contact impedances and the shunting effect on the

electrode-tissue interface [30, 134]. CEM is defined by the governing equation

$$\nabla \cdot (\sigma \nabla u) = 0, u \in \Omega, \tag{3.6}$$

where σ is the conductivity distribution, u the electric potential distribution, x an arbitrary point, and Ω the volume conductor. In CEM, the voltage of the electrodes and electrical current behaviour on the boundary are determined by

$$u + z_l \sigma \frac{\partial u}{\partial v} = U_l, x \in e_l, l = 1,2, \dots, L \tag{3.7}$$

$$\int_{e_l} \sigma \frac{\partial u}{\partial v} ds = I_l, x \in e_l = 1,2, \dots, s \tag{3.8}$$

$$\sigma \frac{\partial u}{\partial v} = 0, x \in \Omega \setminus \bigcup_{l=1}^{L} e_l \tag{3.9}$$

where z_l is the effective contact impedance on l'th electrode e_l, v the outward unit normal of the boundary of the volume conductor, U_l the measured potential on the l'th electrode, s the boundary of the electrode, L the number of electrodes, and I_l the injected current on the l'th electrode. Further, for a unique solution

$$\sum_{l=1}^{L} I_l = 0 \tag{3.10}$$

and

$$\sum_{l=1}^{L} U_l = 0 \tag{3.11}$$

are required.

3.3 BIOIMPEDANCE APPLICATIONS

Major application areas of bioimpedance measurements are dynamic measurements in impedance cardiography (ICG) and impedance pneumography. ICG is based on the measurement of varying impedance due to changes in blood volume and flow in the thorax following cardiac contraction (Figure 3.3) [113]. Blood has low impedivity in contrast to other tissues; thus, an increased amount of blood in the thorax following the systole can be detected as a decrease of the impedance of the thorax [113] (Figure 3.3B). ICG can be used in non-invasive detection of stroke volume, cardiac contractility, diastolic dysfunction, arrhythmias and systolic time intervals [13, 23, 81, 83, 113].

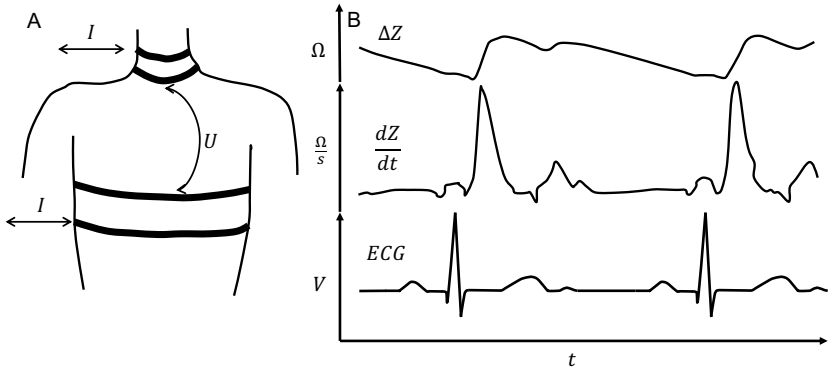

Figure 3.3: *Conventional ICG measurement configuration with one strip electrode pair for current injection I and voltage measurement U (A). An impedance cardiography signal is typically presented as the change of impedance ΔZ, in which the decrease of impedance is conventionally illustrated as upward deflection, or the time derivative of impedance $\frac{dZ}{dt}$ [113] (B). In B an ECG signal is provided as a temporal reference. Figure modified from [113].*

Impedance pneumography is used to monitor respiratory function with transthoracic bioimpedance measurements (Figure 3.4). The measurement reflects the varying lung air content [10, 56]. In addition, everything that has an effect on the current pathways in the thorax during respiration, that is, the change in thorax shape and organ motion, affects impedance pneumography measurement [10, 12, 92]. As

the signal is measured essentially from the same location as ICG, signal processing is required to eliminate cardiogenic oscillation to obtain a smooth respiratory signal (Figure 3.4). Impedance pneumography applications include apnoea detection and respiratory flow measurements as well as monitoring of intrathoracic fluid accumulations such as lung oedema [10, 52, 128, 163].

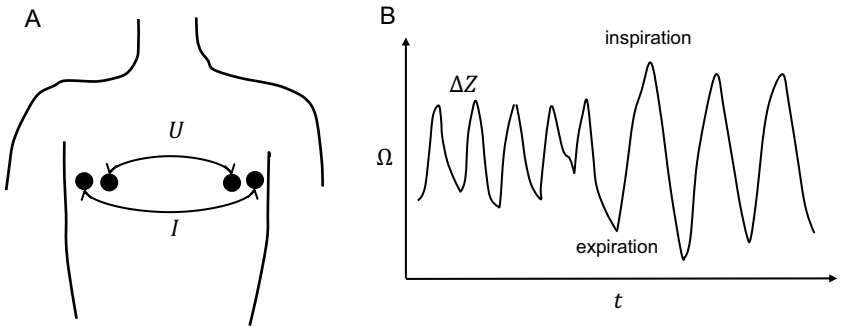

Figure 3.4: *Horizontal impedance pneumography measurement configuration using one pair of current injection I and voltage measurement U spot electrodes (A). The impedance change signal ΔZ can be used to monitor the respiratory phase (B).*

Other applications of bioimpedance include impedance spectroscopy techniques, which can be potentially used for measuring body composition in neonates and athletes and as a tool in nutritional and epidemiologic research [21, 66, 88, 100]. Further, image-producing electrical impedance tomography (EIT) methods have been introduced for the monitoring of ventilation, blood perfusion and gas exchange in the lungs [1], for example. Some specific applications of EIT include mammographic imaging as well as evaluation of intrathoracic fluid accumulations and regional lung ventilation [2, 31, 148].

4 Aims of the present study

The main objective of this thesis was to thoroughly evaluate the feasibility of bioimpedance measurements for respiratory and cardiac motion compensation during PET imaging by gating. More specifically, the objectives were divided into four studies:

I To determine an optimized bioimpedance electrode configuration on the upper thorax for simultaneous respiratory and cardiac bioimpedance signal measurement.

II To validate the optimized measurement configuration against reference methods in monitoring respiration and cardiac contractions.

III To evaluate the feasibility of bioimpedance measurement in respiratory gating of oncologic PET imaging using the optimized measurement configuration.

IV To evaluate the feasibility of integrated bioimpedance and ECG measurement in dual gating of cardiac PET using a II bipolar ECG limb lead-based measurement configuration.

5 Materials and methods

This thesis consists of four studies. The first two studies (**I** and **II**) focus on the determination and validation of the bioimpedance measurement configuration. The other two studies concentrate on the evaluation of the bioimpedance-based gating applications in oncologic (**III**) and cardiac (**IV**) PET studies. All the study data is original.

5.1 MEASUREMENT SENSITIVITY OPTIMIZATION

The measurement sensitivity optimization study (**I**) was conducted using a finite element method (FEM) model of a normal-weighted male upper thorax, which was based on CT images. The model consisted of 36,819 tetrahedral elements and contained general tissue, the lungs, the heart and the spine (Figure 5.1), whose electrical properties were characterized by conductivities of 0.1584 S/m, 0.1895 S/m, 0.5200 S/m and 0.0839 S/m, respectively [4, 53]. Further, 54 electrodes (area 430 mm^2, separation 15 mm) were modelled on the anterior surface of the model. The effective electrode contact impedance was matched with the general tissue conductivity, resulting in 0.00545 Ωm^2 [30, 149]. An electrical sinusoidal current of 1 mA at 100 kHz was used in the optimization computations.

The measurement sensitivity (S) optimization in this study was based on the forward problem solution. The node-wise sensitivity distribution was computed in discretized form based on the electrical potential fields of the current injection and voltage measurement electrode pairs as well as the Jacobian of the basis functions [145]. The computations were conducted with previously validated algorithms [147, 149].

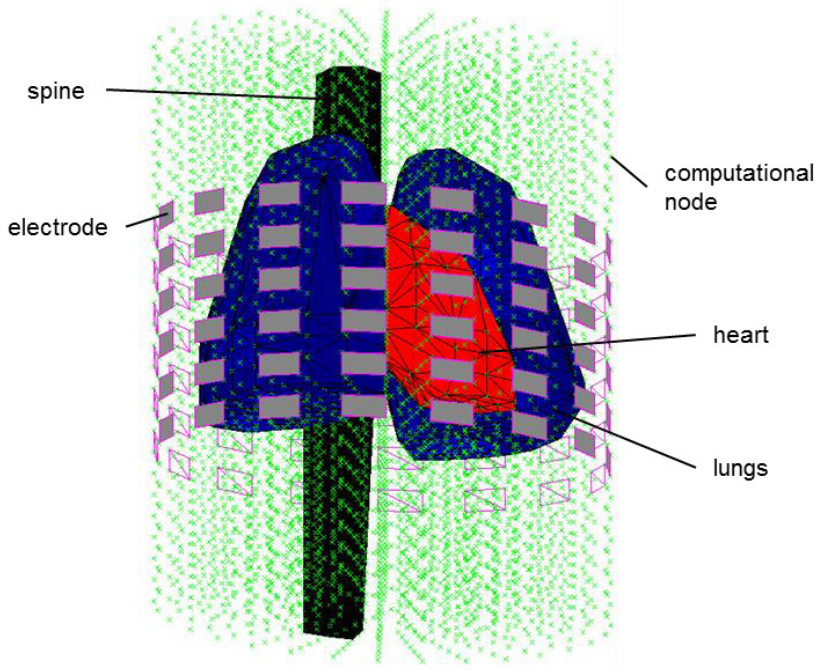

Figure 5.1: *Schematic presentation of the computational model, with the lungs, heart and spine as inhomogeneities.*

The sensitivity for the volume of the lungs and the heart was defined as the sum of the absolute values of nodal sensitivities in the corresponding volumes in altogether 43,792 four-electrode configurations. The consistency of the optimization results through the respiratory and cardiac cycles was further evaluated in the group of the most sensitive configurations by repeating the analyses for 25 different conductivities. In this additional analysis, the conductivities were varied between the inflated and deflated lung (0.10735-0.27161 S/m) as well as the systolic and diastolic heart (0.4590-0.5810 S/m).

5.2 SUBJECTS

All volunteer and patient measurements included in this thesis (Table 5.1) were performed in accordance with the Declaration

of Helsinki. The studies were approved by the Ethical Committee of Kuopio University Hospital, and informed consent was obtained from all subjects. In addition, a declaration on the clinical use of the physiological signal measurement equipment was made to the Finnish National Supervisory Authority for Welfare and Health. The electrical safety of the measurement equipment was verified by the Medical Device Service and Maintenance Unit of Kuopio University Hospital prior to the measurements.

Twelve healthy volunteers were recruited from the staff of Kuopio University Hospital and the University of Eastern Finland for the verification and validation of the optimized bioimpedance measurement configuration. Six of these subjects were included in study **I** as test subjects. The whole study population was included in study **II**.

Table 5.1. *Subject demographics. The values are presented as mean ± standard deviation. BMI = body mass index, F = female, M = male.*

Study	N (F/M)	Age [y]	BMI [kg/m^2]
I	6 (3/3)	41.2 ± 12.7	24.5 ± 3.4
II	12 (6/6)	40.1 ± 12.8	24.6 ± 3.0
III	11 (4/7)	64.5 ± 10.0	26.2 ± 5.0
IV	11 (6/5)	66.2 ± 10.5	24.4 ± 3.7

In study **III**, 12 patients who were referred to an oncologic whole body ^{18}F-FDG or ^{18}F-FDOPA (^{18}F-flourodihydroxyphenylalanine) PET/CT scan due to suspected disease in the lungs or upper abdomen were recruited for the study. However, one patient was excluded from the analysis as all the parts of the study could not be finished due to a clinical schedule conflict.

For study **IV**, 25 patients referred to either myocardial viability, cardiac sarcoidosis or oncologic ^{18}F-FDG PET study were recruited. Thirteen of these patients were excluded from the analyses due to absent, very low or non-uniform uptake. One patient was excluded from the analysis due to unsuccessful bioimpedance measurement, in which the respiratory

component was very small and reliable respiratory gating was prevented by a large cardiac component.

5.3 PHYSIOLOGICAL SIGNAL MEASUREMENTS

All physiological signals in the studies (**I**-**IV**), except for the clinically used respiratory gating signal in study **III**, were acquired with an MP150 based modular measurement device (Biopac Systems, Goleta, CA, USA).

In healthy volunteer measurements for studies **I** and **II**, ECG and lung volume signals were recorded via an MP35 system (Biopac Systems, Goleta, CA, USA) (Figure 5.2A, Table 5.2). Bioimpedance signals were recorded using an EBI100C electrobioimpedance amplifier (Biopac Systems, Goleta, CA, USA) with a 400 μA current feed at 100 kHz. All measurement signals were routed via an MP150 system to enable simultaneous sampling (Figure 5.2A). Bioimpedance signals were recorded with three different electrode configurations determined in the sensitivity optimization study (**I**) (Figure 5.3A-C). However, the optimized configuration was slightly modified by shifting it downward and moving the electrodes on the right side lateral to the mamillae (Figure 5.3A). This was done in order to obtain an electrode placement which could be applied similarly for female and male subjects. ECG signals were recorded from the II bipolar limb lead utilizing MP35. ECG electrodes were located on the right and left clavicular fossa and on the left iliac crest. The respiratory volume was derived via the MP35 by integrating the respiratory flow signal. This signal was recorded with a facemask, a heated pneumotachograph (PNT) (A Fleisch No. 3, Lausanne, Switzerland) and an SS40L differential pressure sensor (Biopac Systems, Goleta, CA, USA). The measurements were conducted with the subject in the supine posture for each bioimpedance measurement configuration. The subjects followed a predefined three-phased breathing pattern, which consisted of 2 minutes of calm uncontrolled normal breathing, 1 minute of slow (0.1 Hz) and

deep audio-instructed breathing as well as 1 minute of fast (0.333 Hz) audio-instructed breathing.

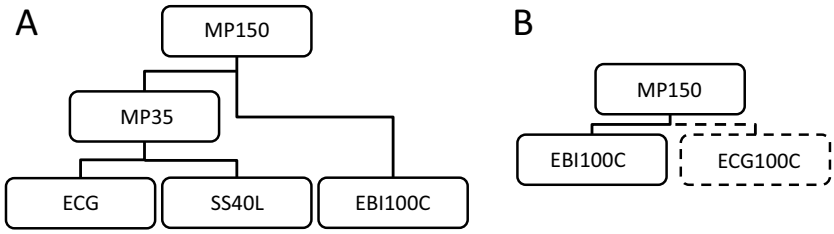

Figure 5.2: *In studies* ***I*** *and* ***II,*** *ECG and respiratory flow were measured with an MP35 system (A). ECG was acquired directly with the MP35, whereas respiratory flow was measured using an SS40L differential pressure sensor. Bioimpedance was measured with an EBI100C electrobioimpedance amplifier. All signals were routed via an MP150 system (A). In studies* ***III*** *and* ***IV,*** *bioimpedance was measured with an EBI100C electrobioimpedance amplifier (B). This measurement set-up was supplemented with the ECG100C for the measurement of ECG in study* ***IV*** *(dashed line in B).*

Table 5.2. *Biopac measurement system acquisition settings with manufacturer-announced nominal cut-off frequencies [18]. All filters are implemented using analog single pole roll-off filters, except for the 65 Hz low pass filter of MP35, which is a digital 2nd order Butterworth filter.*

Study	Signal	Biopac module	High pass	Low pass	Sampling frequency
I & **II**	Bioimpedance[A-C]	EBI100C	None	100 Hz	200 Hz
	ECG	MP35	0.05 Hz	65 Hz	200 Hz
	Lung volume	MP35	None	65 Hz	200 Hz
III	Bioimpedance[A]	EBI100C	None	100 Hz	1 kHz
IV	Bioimpedance[D]	EBI100C	0.05 Hz	100 Hz	1 kHz
	ECG	ECG100C	0.05 Hz	35 Hz	1 kHz

Superscripts A-D denote measurement configurations presented in Figure 5.2.

In study **III**, bioimpedance was measured with similar settings as in **I** and **II** (Table 5.2) using the optimized electrode configuration determined in study **I** (Figure 5.3A) and the EBI100C amplifier (Figure 5.2B). Parallel with the Biopac system, the respiration of patients was recorded with the Real-Time

Position Management (RPM) system, which tracks the vertical displacement of a box with reflective markers using an infrared tracking camera at a sampling frequency of 40 Hz. The box was placed on the thorax, on the location of largest motion.

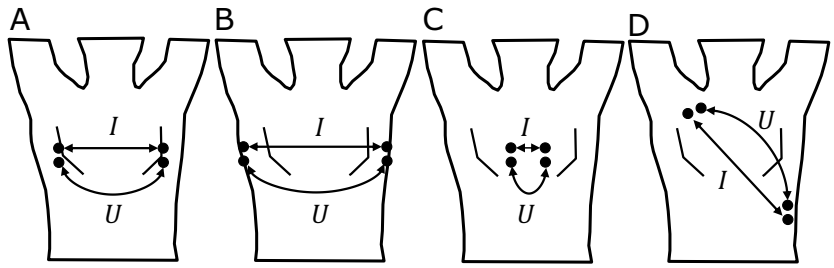

Figure 5.3: *Schematic representation of measurement electrode locations in the optimized configuration (A) as well as in the most sensitive configurations for respiratory (B) and cardiac (C) measurement. Configurations A-C follow from the results of study* ***I****. Configuration D mimics II limb lead ECG locations. Current injection and voltage measurement electrodes are marked with I and U, respectively.*

In study **IV**, both bioimpedance and ECG were measured from the same four electrodes that were located in the proximity of the right clavicular fossa and on the left flank on the level of the lowest ribs, thus mimicking the II limb lead configuration (Figure 5.3D). The current feed was the same as in studies **I**-**III**. Bioimpedance and ECG measurement leads were attached to common electrodes with custom-made cable connectors (Tuomo Savolainen, Department of Applied Physics, University of Eastern Finland). Bioimpedance and ECG signals were recorded with the EBI100C and ECG100C bioimpedance and electrocardiogram amplifiers (Table 5.2, Figure 5.2B).

5.4 CLINICAL PET STUDIES

In study **III**, the PET/CT image data was acquired with a Discovery D690 scanner (GE Medical Systems, Milwaukee, WI, USA) at the Turku PET Centre, Turku University Hospital. The scanner was equipped with a 64-slice CT and 157 mm axial field

of view in PET. The clinical study, to which the patients were referred, was conducted first with 2-minute PET bed positions and a helical low-dose CT (120 kV, 10-80 mA) utilizing Smart mA and Auto mA dose adaptation (GE Medical Systems, Milwaukee, WI, USA). Following the clinical scan, a 10-minute list-mode (LM) acquisition was run over one bed position accompanied with a 4D CT (80 kV, 30 mA). PET data was reconstructed with a 3D OSEM algorithm (2 iterations, 24 subsets), which featured corrections for randoms, scatter, attenuation, dead time and normalization. In addition, a 1-4-1 weighted average filter was applied in the axial direction, accompanied by a 6.0 mm Gaussian filter in the transaxial plane. The PET image matrix size was 256 x 256 x 47, and the corresponding pixel size was 2.73 mm x 2.73 mm x 3.27 mm. PET reconstructions were carried out with the GE Research Gating Tool (RGT). All CT data was reconstructed iteratively (AsIR, GE Medical Systems, Milwaukee, WI, USA) into 512 x 512 images. The bioimpedance measurement was run simultaneously with the 10-minute LM PET acquisition and was temporally synchronized with the LM acquisition using external triggers fed to the Biopac system and the PET scanner. The triggers were generated by a custom-made signal generator/delayer (Pekka Tiihonen, Diagnostic Imaging Centre, Kuopio University Hospital). Nine images were reconstructed from each patient. The non-gated, or static, image was the baseline of parameter comparisons. Eight respiratory-gated images were reconstructed using either amplitude- or time-based gating, bioimpedance or the RPM system, or different attenuation correction methods. Attenuation correction in respiratory-gated PET reconstructions was based either on averaged AC maps over the whole respiratory cycle (A-CTAC) or gated AC maps (G-CTAC), which were matched to the respiratory phase of the PET data. The gating of the AC maps was based on RPM measurements in all reconstructions since the bioimpedance measurement device could not be interfaced with the scanner in a patient study.

In study **IV**, the PET/CT image data was acquired with a Biograph mCT scanner (Siemens Healthcare, Erlangen, Germany) at the Department of Nuclear Medicine, Klinikum rechts der Isar der Technischen Universität München; and the Department of Clinical Physiology, Nuclear Medicine and Clinical Neurophysiology, Kuopio University Hospital. The scanner was equipped with a 128-slice CT and had a PET axial field of view of 216 mm. In case the subject was referred to a myocardial viability or cardiac sarcoidosis study, a 20-minute dual-gated list-mode scan over one bed position was acquired as part of the clinical protocol. In case the subject was referred to an oncologic study, a 10- or 20-minute additional LM scan over one bed position was acquired, depending on the physical condition of the patient. PET images were reconstructed using a clinical 3D OSEM algorithm (3 iterations, 21 subsets) with TOF and PSF corrections (UltraHD, Siemens Healthcare, Erlangen, Germany) into transaxial images of 512 x 512 corresponding to a pixel size of 1.59 mm x 1.59 mm to obtain dense sampling for activity line profile measurements. The axial pixel size was 3.0-5.0 mm, depending on the clinical study. No post-reconstruction filter was applied. Attenuation correction was based on a standard low-dose CT of the clinical study, with real-time angular and topogram-based CARE Dose4D (Siemens Healthcare, Erlangen, Germany) dose adaptation (reference voltage 120 kV, reference current 30 mA). CT images (512 x 512) were reconstructed with filtered back projection due to the extended field of view option utilized in the scanner. Bioimpedance and ECG measurements were synchronized with the LM data similarly to study **III**. Four images were reconstructed in study **IV**: static containing all the acquired data as well as respiratory-gated, cardiac-gated and dual-gated; in the last three, the data for the reconstruction was selected according to bioimpedance and ECG measurements.

5.5 DATA ANALYSIS

5.5.1 Signal analysis

All signal analyses were performed with Matlab 2007b (The Mathworks, Inc., Natick, MA, USA).

In the sensitivity optimization study (**I**), the electrode configuration having the highest simultaneous sensitivity in the anatomical volumes of both the lungs and the heart was identified by an exhaustive search. Specifically, it was required that both lungs contribute at least with a proportion of 45% to the overall lung sensitivity to obtain a comprehensive measurement of lung status. In addition, the most sensitive configuration for the volume of the lungs and the most sensitive configuration for the volume of the heart were determined.

Bioimpedance measurements of healthy volunteers were used to evaluate the computational sensitivity optimization results in the time and frequency domains (**I**). Following the preprocessing of the signal with 5th order Butterworth high (0.05 Hz) and low (10 Hz) pass filters and zero-averaging, the respiratory and cardiac components were separated with band pass filters. The respiratory pass band was fixed between 50% of the respiration rate and 90% of the heart rate. The cardiac pass band was fixed between 90% of the heart rate and 10 Hz. In the time domain analysis, the mean peak-to-peak amplitude of the respiratory and cardiac cycles was determined. In the peak-to-peak analysis, cycles visually observed to be clearly deviant were manually excluded. In the frequency domain analysis, the power of the signal was computed as an integral of the periodogram estimate on the respiratory and cardiac pass bands. Both analyses were performed for each configuration and breathing pattern.

In study **II**, respiratory signals acquired with bioimpedance and PNT were compared. Both signals were high-pass filtered (0.05 Hz) to remove baseline fluctuation and drift. A 1000-ms moving average filter was used to smooth the cardiogenic oscillation in the bioimpedance signal in order to separate the respiratory component. The PNT signal was

smoothed with a 5th order Butterworth low-pass filter (0.5 Hz) (Ernst 1999). Further, both bioimpedance and PNT signals were zero-averaged and normalized for comparison. The end-inspiratory and end-expiratory peaks were detected with a constant threshold peak detection algorithm, which enabled the comparison of mutual peak-to-peak amplitudes and durations of respiratory cycles.

A temporal interval comparison was also conducted for cardiac signals. The onsets of the cardiac cycle (Z peaks) were separated from the bioimpedance signal, based on the algorithm by Pan and Tompkins [111]: The cardiac band was separated from the bioimpedance signal by 5th order Butterworth high (0.6 Hz) and low (20 Hz) pass filters, after which the signal was difference-filtered, cubed and moving average (100 ms) filtered. Corresponding events (R waves) were detected from the ECG signal by 5-30 Hz band bass filtering, difference filtering, squaring and moving average (100 ms) filtering the ECG signal. Z peaks and R waves were detected with a constant threshold peak detection algorithm for the evaluation of cardiac interval detection. In addition to correlation and agreement analyses of respiratory and cardiac signals, the temporal consistency of the signals was evaluated by calculating the difference between the observed end-expiratory instants of measured respiratory signals (bioimpedance vs. PNT) as well as Z peaks and R waves (bioimpedance vs. ECG).

In study **III**, the cardiac component was first extracted from the bioimpedance measurement using 5th order Butterworth high (0.6 Hz) and low (20 Hz) pass filters. Subsequently, the respiratory component of the bioimpedance signal was separated by subtracting the cardiac component from the measurement signal. The remaining respiratory signal was smoothed with a 100-ms moving average filter. Non-physiological drift or baseline variation, which occurred in five measurements, was compensated by trend removal. The trend was estimated using a long (50,000 ms) moving average filter. Respiratory bins were determined cycle-wise from the bioimpedance measurement. Largely deviant cycles were

excluded from the binning. In amplitude gating, the cycle deviation from mean peak-to-peak amplitude was not allowed to exceed 2 standard deviations. Further, it was a requisite that the positive and negative peaks of the cycles do not deviate by more than 1 standard deviation from the mean of the respective peaks. In time gating, it was an additional requirement that the cycle duration differ less than two standard deviations from the mean cycle duration. Valid respiratory cycles were divided either to 5 bins of equal height (amplitude gating, Figure 5.4A) or 5 bins of equal duration (time gating, Figure 5.4B). Bioimpedance-based respiratory binning closely mimicked the binning performed by the RPM system, which was used for comparison in this study.

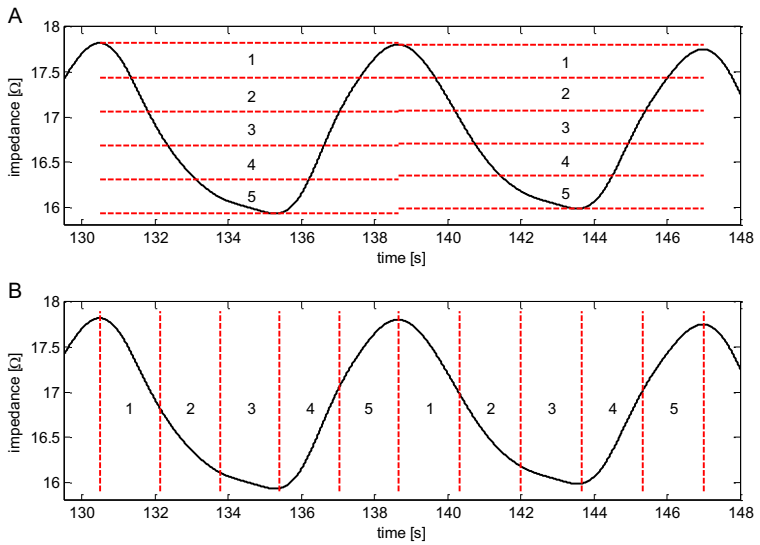

Figure 5.4: *Bin limits in amplitude (A) and time (B) gating of study* ***III****. The respiratory-gated image was reconstructed using the end-expiratory bin, which was bin 5 in amplitude gating and bin 3 in time gating.*

In study **IV**, the respiratory component of the bioimpedance signal was processed similarly to that in study **III**, except for the cardiac pass band, which was 1-20 Hz. The ECG signal processing was performed as in study **II**. The respiratory bins were determined according to global amplitude bins over the whole measurement. As opposed to study **III**, no limits for

cycle characteristics were thus used in study **IV**. On the other hand, the upper limit of respiratory bin 1 was determined by the mean of the detected positive peaks, with one standard deviation added. Similarly, the lower limit of bin 5 was determined as the mean of the detected negative peaks subtracted by one standard deviation. The range between these limits was divided into 5 bins of equal height (Figure 5.5A). Cardiac bins were determined dividing the R-R interval into five equitemporal bins (Figure 5.5B). LM files corresponding to the bins were generated for the reconstruction from the original study LM file by custom-built software (Sebastian Fürst, Department of Nuclear Medicine, Technische Universität München).

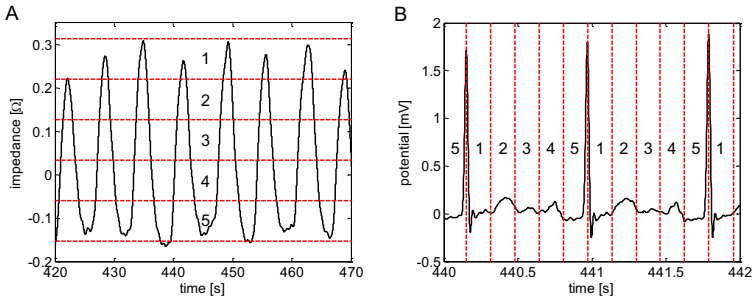

Figure 5.5: *Bin limits in respiratory (A) and cardiac (B) gating used in study **IV**. The respiratory-gated image was reconstructed from the data corresponding to the end-expiratory bin (respiratory bin 5), the cardiac-gated image corresponding to end-diastolic bin (cardiac bin 5) and the dual-gated image corresponding to end-expiration and end–diastole (respiratory bin 5 and cardiac bin 5).*

5.5.2 Image analysis

In study **III**, the peak and maximum metabolic uptake (SUV_{peak} and SUV_{max}), volume (SUV_{vol}), target-to-background ratio (TBR) and displacement of lesions were determined with a clinical AW Workstation (GE Medical Systems, Milwaukee, WI, USA). SUV_{max} was determined as the maximum uptake value of a voxel in the target. SUV_{peak} was determined according to PERCIST criteria in a 1 cm^3 volume sphere centred on the hottest point in the tumour [153]. SUV parameters were normalized according to lean body mass. SUV_{vol} was determined as the

volume of the lesion delineated by the SUV threshold inside the range of 50-70% of SUV_{max}. The percentage threshold was chosen for each patient based on visual assessment of the uptake intensity and surrounding biological uptakes, such as the myocardium, to provide a reliable delineation of the volume. TBR was computed as the ratio of the mean SUV in SUV_{vol} and the mean of the biological background, which was measured on the flank of the patient, where no specific uptake was observed. The SUV-related parameters were determined in end-expiratory bins of amplitude (bin 5) and time (bin 3) gating. The motion between inspiration and expiration was estimated in cranial-caudal (DISP CC) and anterior-posterior (DISP AP) directions by measuring the displacement of the central part of the lesion, defined using a 90% SUV threshold (Figure 5.6). The displacement was measured between bins 1 and 5 in amplitude gating and bins 3 and 5 in time gating.

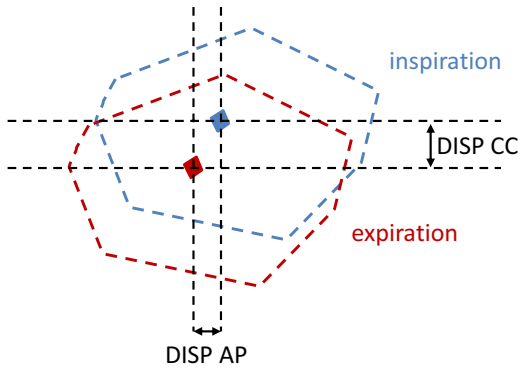

Figure 5.6: *The measurement of the cranial-caudal (DISP CC) and anterior-posterior (DISP AP) displacements of tumours in study* ***III****. Tumour motion between inspiration and expiration was estimated by measuring the displacement of the central part of the tumour (quadrangle), which was delineated using a 90% threshold of the maximum standardized uptake value (SUV_{max}). The volume of the gross tumour is illustrated with a dashed line.*

In study **IV**, the effect of respiratory gating was evaluated in left ventricular volume and myocardial wall thickness measurements. Left ventricular volume was measured using QPS PET software (Cedars-Sinai Medical Center, Los

Angeles, CA, USA). Myocardial wall thickness was measured from lateral wall basal to papillary muscles in three adjacent activity line profiles. Myocardial wall thickness was estimated by the full-width half-maximum (FWHM) of the Gaussian, which was fitted to the line profile. In addition, respiratory-originated cardiac displacement was measured in cranial-caudal, anterior-posterior, and lateral, directions between inspiration and expiration. Displacement was estimated from the peaks of Gaussians, which were fitted into inferior, anterior and lateral myocardial wall activity line profiles in end-inspiration and end-expiration. Further, an estimate for the overall displacement of the myocardium D_0 was calculated as

$$D_0 = \sqrt{D_{CC}^2 + D_{AP}^2 + D_{LAT}^2}, \quad (5.1)$$

where D_{CC}, D_{AP} and D_{LAT} are cranial-caudal, anterior-posterior and lateral displacements, respectively. The activity line profiles were acquired with the HybridViewer software version 2.1 (Hermes Medical Systems AB, Stockholm, Sweden).

5.6 STATISTICAL ANALYSIS

In the studies of this thesis, the normality of the data was tested using the Shapiro Wilk test. As the majority of the data was not normally distributed, non-parametric methods were used in the analyses. The statistical difference between the methods studied was determined using Wilcoxon signed rank sum test (studies **I-IV**). The agreement between bioimpedance-based methods and reference methods, PNT volume spirometry and ECG, was evaluated with a non-parametric modification of Bland-Altman analysis (study **II**) [19]. In addition, Pearson correlation was used to estimate linear association in studies **II-IV**. Statistical analysis was conducted in the IBM SPSS Statistics version 17.0 and 19.0 (IBM Corporation, Armonk, NY, USA) and Matlab 2007b (The Mathworks, Inc., Natick, MA, USA).

6 Results

6.1 THE OPTIMIZED BIOIMPEDANCE CONFIGURATION

In study **I**, three electrode configurations were determined: (1) the optimized electrode configuration having high sensitivity for the lung and cardiac regions as well as a balanced contribution from both lungs to total lung sensitivity. (2) the most sensitive configuration for the lung region with low sensitivity in the cardiac region. (3) the most sensitive configuration for the cardiac region with low sensitivity in the lung region (Table 6.1, Figure 6.1).

Table 6.1: *Sensitivity optimization results. The figures inside brackets in the lung region sensitivity column illustrate the origin of the measurement sensitivity from the left and the right lung, respectively.*

Electrode configuration	**Electrode locations (Figure 6.1)**	**Sensitivity for the lung region [mVm/S]**	**Sensitivity for the cardiac region [mVm/S]**
(1) Optimized	A	78.6 (54% / 46%)	13.9
(2) Lung region	B	105.0 (45% / 55%)	4.6
(3) Cardiac region	C	5.4 (70% / 30%)	13.9

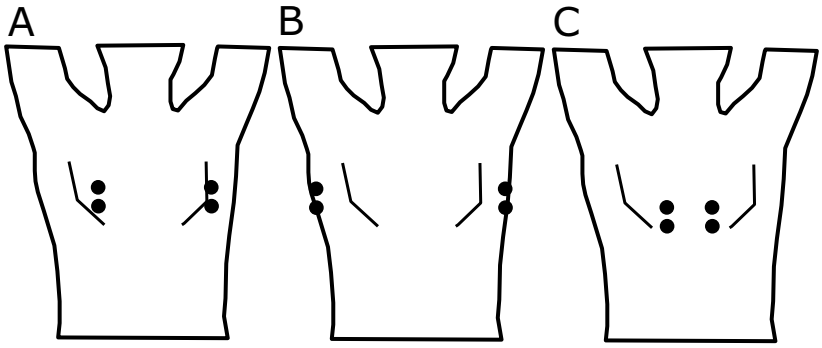

Figure 6.1: *The optimized electrode configuration (A), the most sensitive configuration for the lung region (B) and the most sensitive configuration for the cardiac region (C) as determined in the computational sensitivity study.*

According to the sensitivity computations (Table 6.1), the optimized measurement configuration achieves 75% and 69% of the lung and cardiac region sensitivities, respectively, compared to the specialized configurations for the lung and cardiac regions. Moreover, when the lung and heart sensitivities were altered to simulate possible changes by respiration and cardiac function, the respective relative sensitivities remained high, resulting in 69-79% in lung region sensitivity and 62-78% in cardiac region sensitivity. However, despite the high and balanced contribution of both lungs, the most sensitive measurement volume is on the body surface covering mainly the anterior section of the lungs (Figure 6.2).

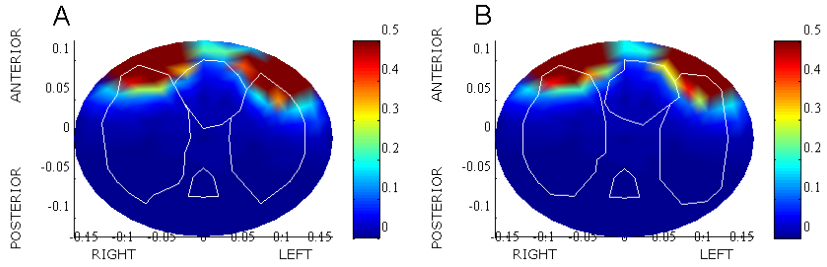

Figure 6.2: *The sensitivity distribution on two transaxial slices between the current injection and voltage measurement electrodes in the computational phantom. The units of the axes and the sensitivity bar are m and mVm/S, respectively. The outlines of inhomogeneities (heart, lungs and spine) are illustrated with white lines.*

6.2 VALIDATION OF THE MEASUREMENT CONFIGURATION

The sensitivity computation results were verified with physiological measurements, which were evaluated in the time and frequency domains (study **I**). Interestingly, the optimized configuration produced significantly higher peak-to-peak amplitudes and frequency content in measurements of both respiration and cardiac function with all breathing patterns when the study population of all 12 volunteers was analysed (Table 6.2, unpublished results).

Table 6.2: *The ratio of mean peak-to-peak amplitude (time domain) and frequency content (frequency domain) between configurations A-C (Figure 5.3) in the analyses of respiratory and cardiac signals in 12 volunteers. The optimized configuration (A) produced significantly (Wilcoxon, $p \leq 0.005$) larger peak-to-peak amplitudes and higher frequency content in all the studied parameters with all respiratory patterns compared to configurations B and C. NORM, SLOW and FAST refer to calm, uncontrolled normal breathing as well as audio-guided slow- and fast-paced breathing.*

	Time domain analysis [%]		**Frequency domain analysis [%]**	
	Respiration	**Cardiac**	**Respiration**	**Cardiac**
B/A, NORM	75	80	59	67
C/A, NORM	46	46	24	20
B/A, SLOW	67	81	45	61
C/A, SLOW	57	46	39	20
B/A, FAST	71	79	50	61
C/A, FAST	50	44	27	18

For respiratory gating applications, it is important that the depth and temporal phase of respiration can be accurately defined. In cardiac gating, the temporal phase is important. The unprocessed transthoracic bioimpedance measurement contains the high-amplitude, low-frequency respiratory component, which is typically dominant; and the low-amplitude, high-frequency cardiac component, which can be separated by signal processing (Figure 6.3). When the optimized measurement configuration was used, the respiratory component was seen to accurately follow the trace of the simultaneously recorded PNT

volume signal (Figure 6.3B). Moreover, respiratory peak-to-peak amplitudes and cycle durations were found to have a high degree of correlation and good agreement between the bioimpedance and PNT measurements (Table 6.3, Figure 6.4). The cardiac signal separated from the measurement by the optimized electrode configuration and properly processed mainly corresponded well with the ECG measurement (Figure 6.3C). In these cases, the intervals between the Z peaks had a high temporal correlation and good agreement with the R-R intervals detected from simultaneous ECG measurements. However, strong occasional suppression of Z peaks was observed in three subjects; this prevented the detection and comparison of cardiac intervals during their occurrence.

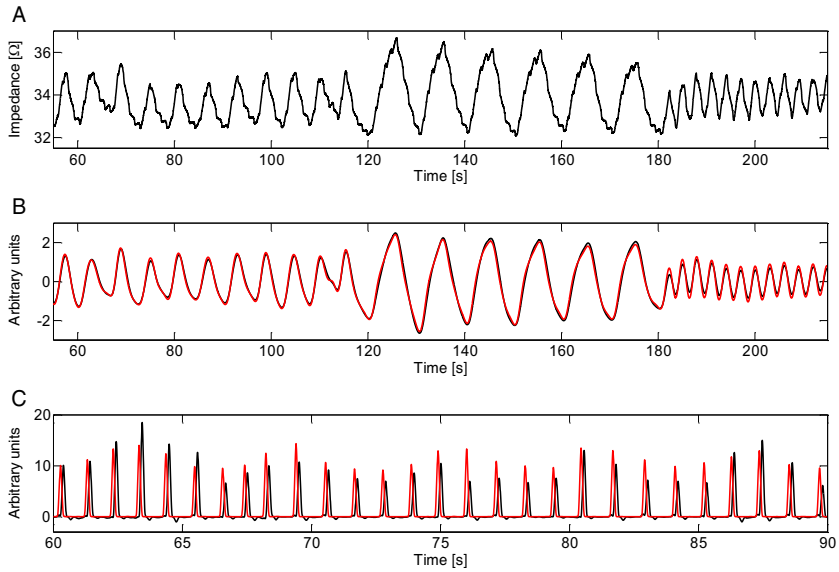

Figure 6.3: *Unprocessed bioimpedance signal (A), separated respiratory component of bioimpedance signal (black line) and PNT volume signal (red line) (B) as well as processed cardiac component of the bioimpedance signal (black line) and processed ECG signal (red line) (C). In B, signals are normalized for comparison. In C, signal amplitudes have been matched to facilitate comparison.*

Table 6.3: *Correlation and Bland Altman analysis results for the comparison of the optimized bioimpedance electrode configuration and the reference methods. R_PP, R_CD and C_CD refer to respiratory peak-to-peak amplitudes, respiratory cycle duration and cardiac cycle duration, respectively. NORM, SLOW and FAST refer to uncontrolled normal breathing as well as audio-guided slow- and fast-paced breathing.*

Parameter	**Linear correlation**	**Mean difference**	**Lower 95% limit of agreement**	**Upper 95% limit of agreement**
R_PP NORM	r = 0.949	-2.6%	-19.2%	14.2%
R_PP SLOW	r = 0.961	1.0%	-7.3%	10.4%
R_PP FAST	r = 0.944	-19.5%	-32.2%	-4.5%
R_CD NORM	r = 0.999	0.7 ms	-75 ms	75 ms
R_CD SLOW	r = 0.998	-2.5 ms	-240 ms	185 ms
R_CD FAST	r = 0.971	-0.4 ms	-65 ms	55 ms
C_CD NORM	r = 0.998	0.03 ms	-20 ms	20 ms
C_CD SLOW	r = 0.997	0.1 ms	-20 ms	20 ms
C_CD FAST	r = 0.971	3.8 ms	-40 ms	25 ms

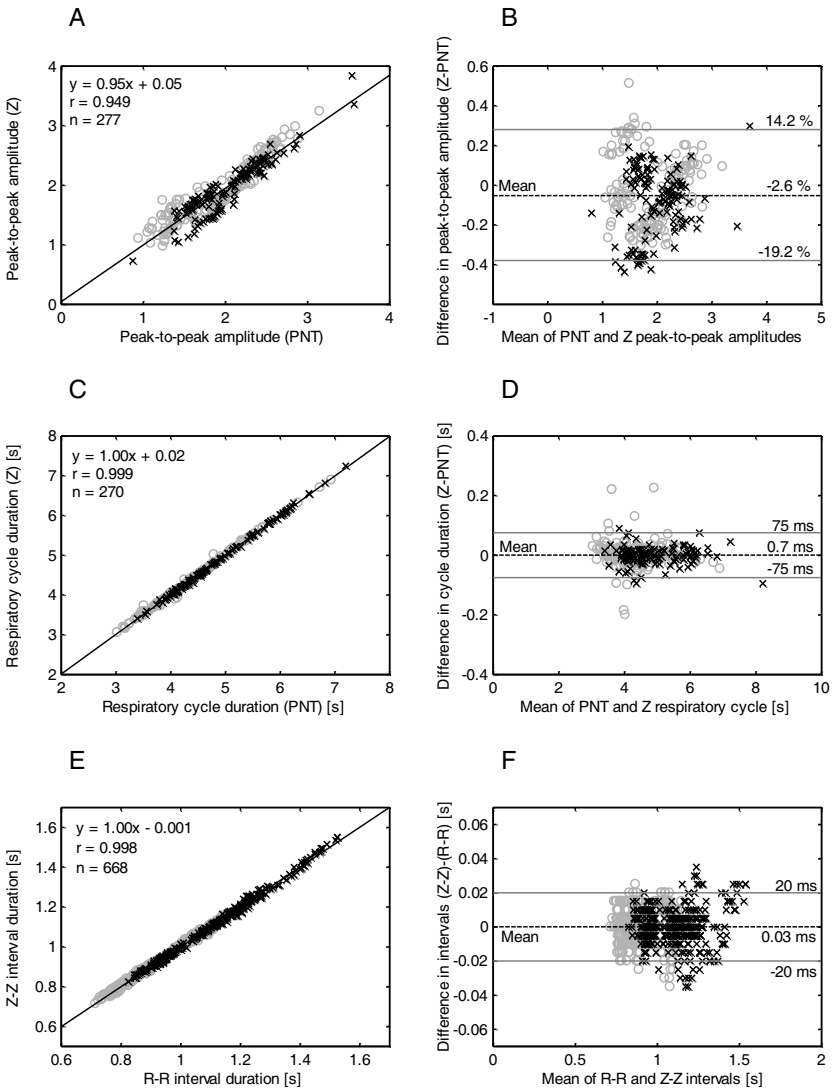

Figure 6.4: *Correlation (A, C, E) and Bland-Altman (B, D, F) plots of normalized respiratory peak-to-peak amplitudes (A, B), respiratory cycle duration (C, D) and cardiac cycle duration (E, F) between the bioimpedance and reference methods. In the Bland-Altman plots, the bias between the methods is presented with a dashed black line. The solid grey lines illustrate the 95% limits of agreement.*

6.3 BIOIMPEDANCE-BASED RESPIRATORY GATING IN ONCOLOGIC PET

In the oncologic PET study (**III**), 15 lesions were analysed for SUV_{max}. Of these, 13 were analysed for SUV_{vol}, TBR, DISP CC and DISP AP and 11 for SUV_{peak}. Two lesions were excluded due to their shape, which prevented reliable volume measurement and another two as they did not meet the size criteria of PERCIST for SUV_{peak}.

Bioimpedance-based respiratory gating generally enhanced the visibility of lesions with both amplitude- and time-based gating. The edges of lesions became sharper, and especially small lesions could be observed more easily (Figure 6.5).

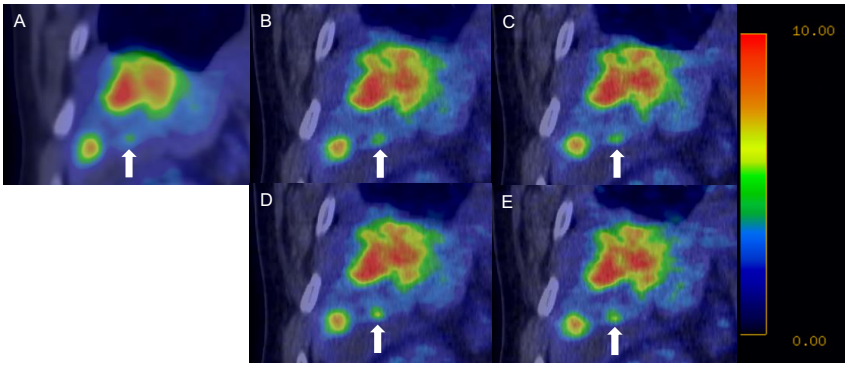

Figure 6.5: *Non-gated (A), amplitude- (B) and time-based (C) RPM-gated as well as amplitude- (D) and time-based (E) bioimpedance-gate PET/CT images of a patient with liver lesions. The patient was imaged with ^{18}F-FDG. In the gated images, the outlines of the uptakes are sharper and more detailed. The effect of gating is seen specifically as the improved visibility of the small lesion (white arrow). SUV_{max} of the small lesion is 4.2 in A, 4.8 in B, 5.6 in C, 6.4 in D and 6.1 E. In this case, bioimpedance gating results in higher increase in visibility and SUV_{max} than the RPM method.*

In the study population, a 6.0-6.8 mm and 1.9-2.6 mm mean displacement of the target lesion was observed in the cranial-caudal and anterior-posterior directions using bioimpedance-based respiratory gating (Table 6.4). Respiratory motion compensation by bioimpedance-based respiratory

gating led to a significant increase ($p \leq 0.05$, Wilcoxon) in SUV_{peak}, SUV_{max} and TBR compared to the non-gated image using all studied gating methods (Table 6.4, Figure 6.6A). On the other hand, the AC technique, based either on A-CTAC or G-CTAC, had a minor, non-significant, effect on SUV_{peak} (Figure 6.6A), SUV_{max} and TBR. Compared to the non-gated study, the decrease of SUV_{vol} was significant in all the gating methods, except for the amplitude-based gating with G-CTAC (Table 6.4, Figure 6.6B). Similarly to SUV-related parameters, the two AC techniques applied did not have a significant effect on SUV_{vol}.

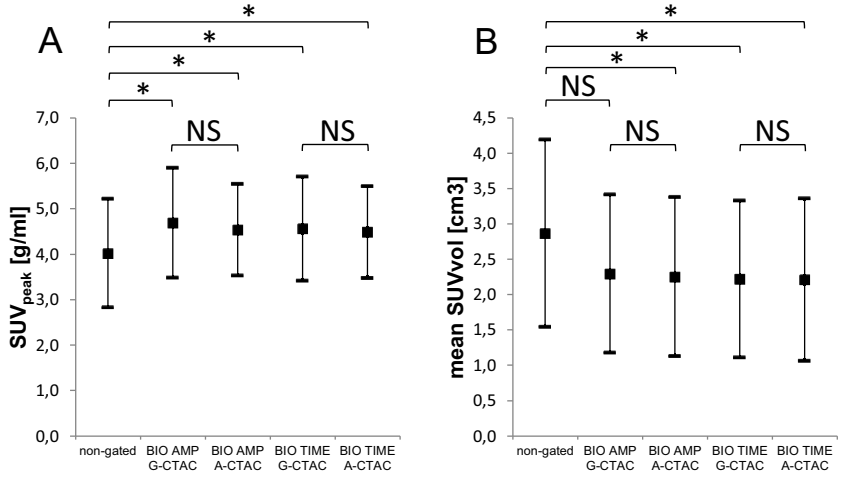

Figure 6.6: *Mean SUV_{peak} (A) and SUV_{vol} (B) in the non-gated study and bioimpedance-gated studies. Standard deviations of measurements and statistical significances of differences are illustrated with error bars and square brackets, respectively. * refers to a statistically significant ($p \leq 0.05$) and NS to non-significant difference. BIO, AMP and TIME refer to bioimpedance-, amplitude-and time-based gating. G-CTAC and A-CTAC refer to computed tomography-based attenuation correction, which is based on averaged and gated 4D CT.*

Table 6.4: *Observed displacement of target lesion in cranial-caudal (DISP CC) and anterior-posterior (DISP AP) directions as well as changes of studied parameters against the non-gated baseline image using different gating methods and attenuation correction principles. The results are presented as mean ± standard deviation.*

Image series	DISP CC [mm]	DISP AP [mm]	SUV_{peak} [%]	SUV_{max} [%]	SUV_{vol} [%]	TBR [%]
BIO AMP G-CTAC	6.8 ± 4.3 mm	2.6 ± 2.2 mm	22.9 ± 44.5	21.6 ± 34.7	-16.5 ± 25.6	23.2 ± 40.4
RPM AMP G-CTAC	7.0 ± 4.9 mm	2.1 ± 2.1 mm	22.3 ± 42.5	21.4 ± 29.4	-15.9 ± 26.5	22.4 ± 35.5
BIO AMP A-CTAC	6.8 ± 4.3 mm	2.6 ± 2.2 mm	18.9 ± 37.7	19.8 ± 31.6	-18.0 ± 25.5	22.7 ± 36.9
RPM AMP A-CTAC	7.1 ± 5.1 mm	2.1 ± 2.1 mm	21.4 ± 36.9	20.1 ± 26.1	-16.0 ± 25.6	21.1 ± 32.4
BIO TIME G-CTAC	6.0 ± 4.1 mm	1.9 ± 1.7 mm	19.8 ± 45.3	24.1 ± 38.2	-20.7 ± 18.2	24.6 ± 43.9
RPM TIME G-CTAC	3.7 ± 4.4 mm	1.9 ± 1.6 mm	15.6 ± 40.7	20.1 ± 31.0	-19.5 ± 29.5	19.0 ± 35.0
BIO TIME A-CTAC	6.0 ± 4.1 mm	2.0 ± 1.8 mm	17.7 ± 39.1	22.0 ± 33.7	-20.8 ± 20.7	21.5 ± 38.2
RPM TIME A-CTAC	3.7 ± 4.1 mm	2.4 ± 1.8 mm	13.2 ± 35.8	17.9 ± 25.9	-17.5 ± 29.7	17.7 ± 30.0

Compared to the clinically widely used RPM respiratory gating method, the differences between the methods were non-significant in all the parameters studied (Figure 6.7). In addition, an excellent correlation (r^2 = 0.87-0.99) was observed in SUV_{peak} (Figure 6.8A, unpublished results), SUV_{max} and TBR between the methods. In SUV_{vol} measurements, the correlation in amplitude-based gating schemes was higher (r^2 = 0.95) (Figure 6.8B) than in time-based gating (r^2 = 0.68-0.74).

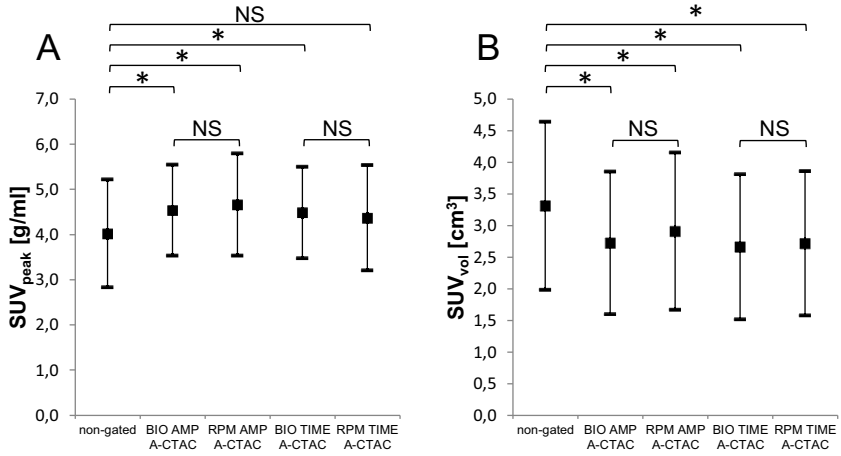

Figure 6.7: *The difference between bioimpedance (BIO) and RPM gating methods was non-significant in the parameters studied. Here, SUV_{peak} and SUV_{vol} with averaged CT-based attenuation correction (A-CTAC) are presented as an example. The use of A-CTAC in the comparison rules out the possible bias caused by the gated attenuation correction (G-CTAC). * refers to a statistically significant ($p \leq 0.05$) and NS to a non-significant difference. BIO, RPM, AMP and TIME refer to bioimpedance-, RPM-, amplitude- and time-based gating, respectively.*

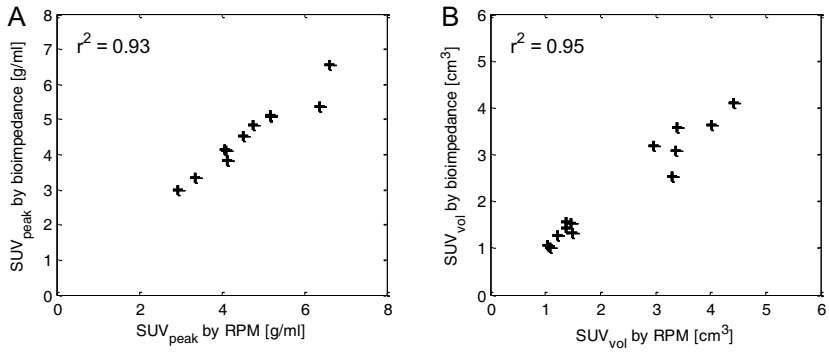

Figure 6.8: *Scatter plots illustrating good correlation in measurements of SUV_{peak} and SUV_{vol} between bioimpedance- and RPM-based gating using A-CTAC.*

6.4 COMBINED BIOIMPEDANCE-BASED RESPIRATORY AND ECG-BASED CARDIAC GATING IN CARDIAC PET

In the cardiac PET study population (study **IV**), in the case of one patient, the bioimpedance measurement was unsuccessful. The respiratory component of the bioimpedance signal measurement was very small, and the large cardiac component prevented reliable respiratory gating (Figure 6.9). Thus, this patient was excluded from the analysis, and the analysis was performed with eleven patients.

In the eleven patients of this study, the observed linear mean myocardial displacement due to respiration was 6.0 ± 2.9 mm in the cranial-caudal, 2.3 ± 1.4 mm in the anterior-posterior, and 2.6 ± 1.8 mm in the lateral, directions. The estimated overall respiratory displacement of the myocardium was 7.6 ± 3.3 mm.

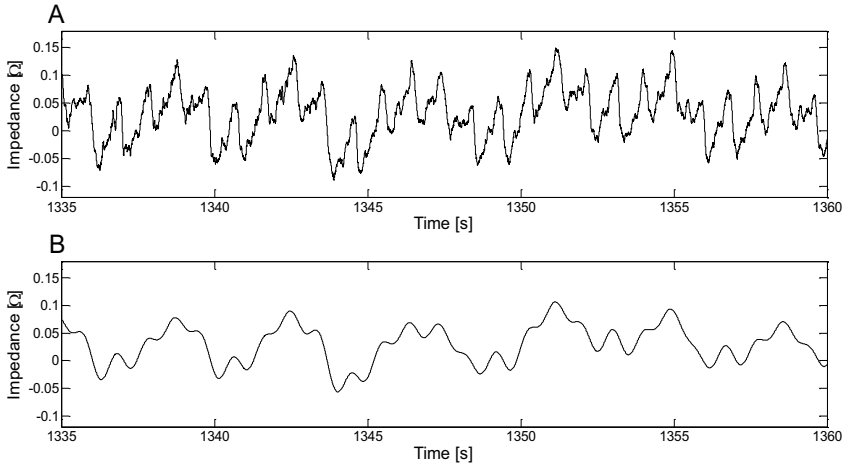

Figure 6.9: *The unprocessed bioimpedance measurement signal (A) and processed respiratory gating signal in the case of unsuccessful bioimpedance measurement, in which the respiratory component was very small and a large cardiac component prevented reliable respiratory gating.*

The left ventricular volume showed a statistically significant ($p < 0.05$, Wilcoxon) 4 ± 3 ml decrease between the cardiac- and dual-gated images and a statistically non-significant 4 ± 5 ml decrease between the static and respiratory-gated images (Table 6.5). However, in the example volume curves of two patients with the highest myocardial uptake, minor differences were seen between the cardiac- and dual-gated image sets (Figure 6.10). The study population for the analysis of the left ventricular volume was limited to six patients as five patients had an uptake too low to enable consistent delineation of the myocardium in all the image series.

Table 6.5: *Left ventricular volumes (LVVs) and myocardial wall thicknesses (MWTs) in the cardiac PET study population. The results are presented as mean ± standard deviation.*

Parameter	static	respiratory	cardiac	dual
LVV [ml]	110 ± 69	114 ± 73	138 ± 78	141 ± 79
MWT [mm]	14.9 ± 2.8	14.4 ± 2.7	11.3 ± 1.3	9.3 ± 1.3

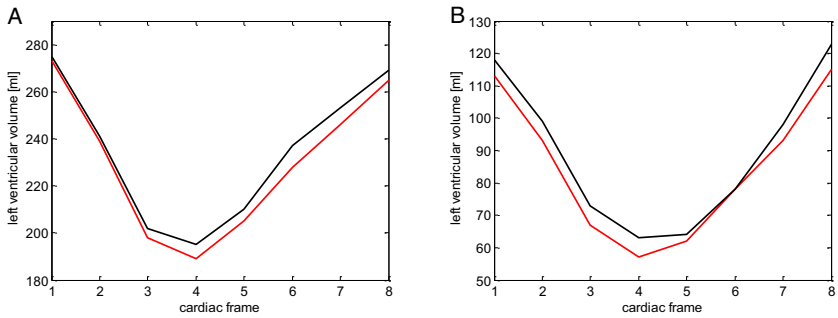

Figure 6.10: *The form of cardiac-gated (red line) and dual-gated (black line) left ventricular volume curves are similar in the two patients with the highest myocardial uptake. In case A, the stroke volume and ejection fraction are 84 ml and 31% in cardiac gating and 80 ml and 29% in dual gating. In B, these measures are 58 ml (50%) and 60 ml (49%), respectively. The main distinction between the curves can be seen in the offset.*

Combined bioimpedance- and ECG-based dual gating had a significant ($p < 0.05$, Wilcoxon) effect on the narrowing of the observed myocardial wall thickness compared to plain cardiac gating (Table 6.5, Figure 6.11A). In addition, the narrowing caused by dual-gating had a considerable correlation ($r^2 = 0.58$) with the estimated overall displacement of the myocardium (Figure 6.11B). Bioimpedance-based respiratory gating alone, on the other hand, had a statistically significant ($p < 0.05$, Wilcoxon) but small effect on the narrowing of the observed myocardial wall thickness compared to static, non-gated images (Table 6.5, Figure 6.11A).

Despite the statistically significant effect of dual-gating on left ventricular volume and myocardial wall thickness, the visual effect may not be as clear. Compared to cardiac gating, dual gating reduces blur and may assist in the distinguishing of structures (Figure 6.12).

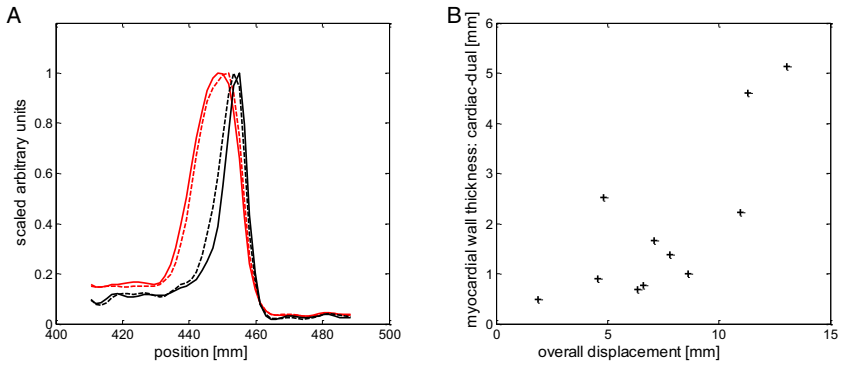

Figure 6.11: *Myocardial wall activity profile as measured from static (solid red line), respiratory-gated (dashed red line), cardiac-gated (dashed black line) and dual-gated (solid black line), images (67 year-old female patient) (A). The scatter plot of overall displacement and the difference in myocardial wall thickness between dual- and cardiac-gated images (B).*

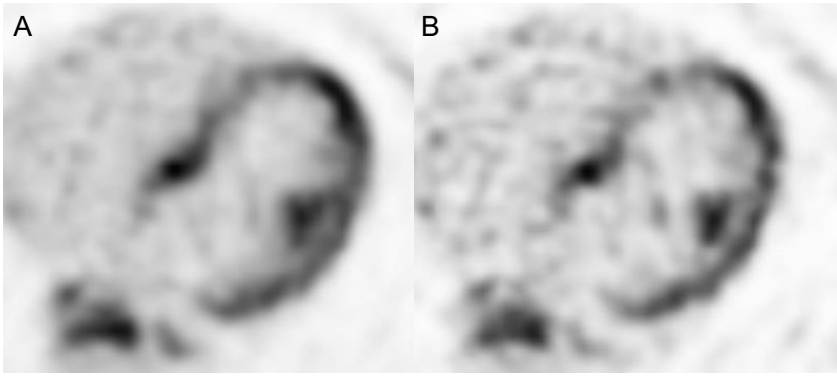

Figure 6.12: *Transaxial slice of the cardiac- (A) and the dual-gated (B) ^{18}F-FDG study. The myocardium and the papillary muscle are more precisely delineated in the dual-gated image. In exchange for the reduced blur, the noise is higher in the dual-gated image due to the rejection of coincidence data outside end-inspiration and end-diastole.*

7 Discussion

In this thesis, an optimized bioimpedance measurement configuration for the simultaneous measurement of the anatomic volumes of the lungs and the heart was determined according to measurement sensitivity analysis (**I**). Further, the optimized measurement configuration was validated against two reference methods, PNT spirometry and ECG in the monitoring of respiration and cardiac contractions (**II**). Finally, the feasibility of bioimpedance–based respiratory measurements for the gating of PET was evaluated in a clinical setting. Plain respiratory gating was studied in oncologic PET using the optimized measurement configuration (Figure 5.3A) (**III**). The simultaneous use of bioimpedance-based respiratory gating and ECG-based cardiac gating was evaluated using the II limb lead mimicking measurement configuration in cardiac PET (Figure 5.3D) (**IV**).

7.1 DETERMINATION AND VALIDATION OF THE OPTIMIZED BIOIMPEDANCE MEASUREMENT CONFIGURATION

According to the measurement sensitivity analysis (study **I**), the optimized electrode configuration was located on the anterior upper thorax at the height of the 4th and 5th intercostal spaces in the proximity of the mamillae (Figure 6.1A). This is a plausible intermediate estimate as, similar to study **I**, it has been reported that high sensitivity in cardiac bioimpedance measurements is achieved with regional measurements in the proximity of the heart [70] and that lateral configurations are most suitable for respiratory bioimpedance measurements [93, 126, 129]. However, direct comparison to other studies on optimizing simultaneous respiratory and cardiac measurement into one measurement configuration cannot be made as, to the

best of the present author's knowledge, there are no other studies on the topic.

The measurement sensitivity of the optimized configuration was high compared to the most sensitive configurations for the lungs and the heart, resulting in 75% and 67% proportional sensitivity, respectively. In addition, the proportional sensitivities for both lung and heart volumes remained high (> 62%) throughout the respiratory and cardiac cycles as estimated by conductivity variation. The high measurement sensitivity of the optimized measurement configuration was verified in physiological measurements with volunteers (study **I**). Partly inconsistent with the computational modelling, the slightly modified optimized measurement configuration (Figure 5.3A) was found to produce superior, significantly larger peak-to-peak amplitudes and higher frequency content in the monitoring of both respiration and cardiac function when compared to configurations which were determined solely for respiratory (Figure 5.3B) and cardiac measurements (Figure 5.3C) (study **I**). However, the approach of measurement sensitivity and time as well as frequency domain analyses is slightly different. Measurement sensitivity (equation 3.4) analysis shows what configuration should be used to measure the highest voltage change for an incremental conductivity change in a certain conductivity distribution. On the other hand, time and frequency domain analyses reflect the impedance change during the whole course of the respiratory and cardiac cycles.

The limitation of the computational sensitivity optimization study is the simplicity of the model: the model is static, and the dynamic changes of thorax geometry or the motion of the internal organs during respiration have not been directly modelled. However, the effect of dynamic changes was evaluated by altering lung and heart conductivities as it has been suggested that the effect of organ movements can be approximated by varying tissue conductivities [146]. Another limitation in the model was the lack of modelled haemodynamics or blood perfusion, for example in lung tissue.

The lungs and the aorta have, nonetheless, been reported to have an important role in ICG measurement [83, 114]. The lack of haemodynamics and lung perfusion modelling may have resulted in some bias in favour of electrode configurations in the vicinity of the anatomical location of the heart when cardiac measurement sensitivity was considered. These aspects may have also contributed to the inconsistencies observed between the results of the modelling part and the physiological measurement part in study **I**.

The results of the optimized measurement configuration validation study (**II**) show that bioimpedance-based respiratory and cardiac measurements have an excellent linear correlation with reference methods in peak-to-peak amplitude (respiratory measurements) and physiological cycle duration (respiratory and cardiac measurements) during three different breathing patterns. According to the Bland Altman analysis, the bias between the measurements was generally small and the limits of agreement were adequately narrow. With each parameter studied, the largest bias and the widest limits of agreement were found either during slow- or fast-paced breathing (Table 6.3). On the other hand, slow- and fast-paced breathing represent extreme breathing conditions. In slow-paced breathing, volunteers breathed utilizing their whole vital capacity. This is not typical during image acquisition, except possibly in single breaths. Fast-paced breathing, on the other hand, was found to be very fast when volunteers tried to maintain their normal breathing depth.

In addition to the correlation and agreement results, there was good temporal agreement between the bioimpedance and reference methods. The time instants of positive respiratory peaks differed on average 45 ms between the measurement methods, which is approximately 1% of the mean interval length observed in the study (4.6 s). In cardiac measurements, the Z peaks were detected on average with a 128 ± 20 ms delay compared to the R waves of the ECG measurement. This follows from the fact that R waves originate from the spreading electrical activity in the heart and Z peaks represent the flow

and distribution of blood following the contraction. The deflection, which in this study is termed Z peak, has been timed to follow the first heart sound, which is related to the closing of atrioventricular valves, and to precede aortic closure [83].

The findings of study **II** are corroborated by other reports. There are other studies, albeit implemented with different measurement configurations, which have reported that bioimpedance measurements can be used for the monitoring of respiration [48, 64, 129]. In addition, there are studies which suggest that bioimpedance measurements can be utilized in the determination of temporal cardiac events [13, 83]. Despite the temporal accuracy of cardiac bioimpedance measurements, the suppression of Z peaks, which occurred in three patients in study **II**, was identified as a potential limitation, considering the use of bioimpedance in cardiac-gating applications. Since ECG signals are excellent in providing information on the instant of cardiac contraction and are in everyday use in clinics, ECG was chosen as the cardiac gating method in study **IV**.

7.2 EVALUATION OF BIOIMPEDANCE-BASED TECHNIQUES IN RESPIRATORY AND DUAL GATING OF PET

The bioimpedance-based respiratory measurement technique was found feasible in quantifying respiratory-induced displacement of lesions and the myocardium during PET imaging using the optimized (**III**) and the II limb lead mimicking (**IV**) measurement configuration, respectively. In both the oncologic (**III**) and cardiac (**IV**) PET studies, very similar mean displacements were found for lesions and the myocardium in the cranial-caudal (oncologic 6.0-6.8 mm, cardiac 6.0 mm) and anterior-posterior directions (oncologic 1.9-2.6 mm, cardiac 2.6 mm). The observed displacements are in line with previous reports on detected motion in oncologic [24, 130] and cardiac [27, 91, 96] studies using different gating methods. Importantly, the observed displacement extents are noteworthy, when compared to the approximately 4.4-5.9 mm spatial

resolution of the scanners used [17, 68]. Small differences in reported displacements may result from different gating methods (amplitude or time), gating or reconstruction parameters (number of bins, matrix size, filter), characteristics of respiratory signal measurements (type of measurement, inaccuracies) as well as individual breathing patterns and characteristics of patients, for example.

In the oncologic study (**III**), significantly higher SUV_{peak} (17.7-22.9%), SUV_{max} (19.8-24.1%) and TBR (21.5-24.6%) and lower SUV_{vol} (16.5-20.8%) were observed in bioimpedance-based respiratory-gated oncologic PET studies compared to non-gated studies. Other researchers have reported comparable changes in SUV_{max} and SUV_{vol}, though higher individual changes have also been published [89, 105].

In cardiac studies (**IV**), statistically significant but minor narrowing (4%) of the observed myocardial wall thickness was observed when respiratory-gated images were compared to non-gated images. On the other hand, significant narrowing (17%) was noted when dual- and cardiac-gated images were compared. Compared to the study of Büther et al. [27], which also analysed the effect of respiratory gating on myocardial wall thickness, a clearly smaller mean change was observed between non-gated and respiratory-gated images in study **IV** (0.5 mm vs. 1.8-2.4 mm). Between cardiac- and dual-gated images, the change was similar to the results of Büther et al. [27] (1.9 mm vs. 1.8-2.4 mm). However, it should be noticed that Büther et al. measured the change in the anterior wall, whereas the lateral wall was measured in study **IV**. In addition, Büther et al. utilized more bins (8 vs. 5) and did not use attenuation correction. In the case of cardiac measurements, it should also be considered that the motion is far from rigid and may involve rotation and twist, which may cause uncertainty in linear measurements.

According to the left ventricular volume analysis in study **IV**, the benefit of dual gating over cardiac gating may be limited in the study of left ventricular volume parameters. The analysis of end-diastolic volumes without (cardiac-gated images)

and with (dual-gated images) respiratory gating showed that the mean difference in volumes between these gating methods was approximately 4 ml (3%). The two cases with the highest myocardial radiopharmaceutical uptake further suggest that in the determination of stroke volume and ejection fraction, the difference (2-4 ml, 1-2%-unit) may be even smaller.

Clinically, the largest potential of respiratory gating in PET may be seen in oncologic imaging. Respiratory gating can improve the visibility of lesions, help to define their motion and aid in more accurate delineation of the treatment volume for radiotherapy [86, 122]. Respiratory gating may also improve co-registration between images from PET and other modalities, such as MRI [25]. In addition, respiratory gating methods and devices can be used in more accurate delivery of radiotherapy and avoidance of normal tissues, for example, in non-small cell lung cancer and breast cancer [34, 131]. In cardiac PET studies, the most probable use for respiratory gating is in the study of small targets, such as coronary plaques [43, 140], or the small uptakes in cardiac sarcoidosis.

In study **III**, the use of either averaged or gated CT as the basis for attenuation correction was not found to produce a significant difference in the results. This is corroborated by the finding that attenuation correction which is based on gated CT is more effective in reducing motion artefacts in some but not all cases when compared to attenuation correction which is based on averaged attenuation correction [74].

According to the parameters in the oncologic PET (**III**) study, the bioimpedance method has a good correlation with the widely used RPM method. Interestingly, apart from SUV_{peak} and SUV_{max} in amplitude-based gating with averaged attenuation correction, bioimpedance-based gating produced larger mean changes in the parameters studied compared to the RPM method. However, the differences are minor and statistically non-significant. The differences between bioimpedance and RPM methods in observed lesion displacement were mostly small. However, in time-based gating, a significantly larger

cranial-caudal displacement was observed using bioimpedance gating compared to the RPM method.

In the comparison between the bioimpedance and RPM techniques, it has to be underlined that there is a quintessential difference between them. RPM measures only the vertical displacement of the marker block whereas transthoracic bioimpedance measurement is affected by transthoracic electrical conductivity changes resulting from changing thorax shape and air volume in the lungs as well as shifts in organ positions. In addition, the gating signal processing and formation of bins were not exactly the same in terms of signal processing and cycle rejection criteria, which may also have contributed to the small observed differences between the techniques. On the other hand, in the case of bioimpedance signals, these were adjusted to resemble RPM processing very closely. This was evaluated to ensure a relevant level of similarity in the processing to enable side-by-side evaluation of the bioimpedance and RPM techniques.

7.3 TECHNICAL AND FUTURE ASPECTS OF BIOIMPEDANCE GATING

The separation of respiratory and cardiac components from the bioimpedance signal in studies **I-IV** was performed using division in the frequency space. Further, the respiratory signal was smoothed with a moving average filter (**II-IV**). The drawback of operating in the frequency space is that the harmonics of the respiratory component overlap with the cardiac frequency band [42, 137]. Thus, straightforward filtering in the frequency space may not fully retain the morphology of the respiratory and cardiac components. However, according to the results of the signal validation study (**II**), the form of the signal is adequately preserved though frequency space filtering is used. This is corroborated by Grant et al. [57], who have reported that frequency space division is sufficient for the separation of bioimpedance signal components. However, with

one patient in study **IV**, the filtering proved to be insufficient for the separation of the respiratory component; this led to the exclusion of the patient from the study population. In this case, the cardiac component remained too dominant after signal processing, leading to unsuccessful respiratory gating. One solution to further smooth the signal is to use a moving average filter with a long window as in study **II** (1000 ms). On the other hand, a shorter (100 ms) window was chosen for studies **III** and **IV** in order to minimally affect the morphology of the respiratory waveform. A more effective means for suppressing cardiac oscillations from the respiratory signal might be the use of adaptive filtering based on detected cardiac events, as suggested by Seppä et al. [127], for example.

In some cases in patient studies (**III**-**IV**), the respiratory amplitude was very low. Apart from the one case mentioned above in study **IV**, the low amplitude was still sufficient for respiratory gating. In addition, the inversion of signal was observed in two cases in study **III** and study **IV**. In inverted cases, the association between lung volume and transthoracic impedance change is negative; that is, an increase in lung volume is observed as a decrease of impedance. Signal inversion is a severe case of non-linearity between lung volume and transthoracic bioimpedance changes. Non-linearity is more typically noticed as low measurement sensitivity in shallow respiratory volumes, while in larger volumes the relationship of lung volume and transthoracic impedance change is clear and linear [92, 126]. Interestingly, body mass index has been reported to correlate negatively with lung volume [69]. Lung volume does not necessarily correlate with respiratory depth but as being overweight may decrease respiratory volumes, the probability of non-linear behaviour of bioimpedance measurements may be elevated in overweight patients. It has also been reported that the more caudally the bioimpedance measurement electrodes are located on midaxillary lines, the more prone the measurement is for non-linearity [92, 126]. Considering the occasionally encountered low respiratory amplitudes and signal inversion, a relevant aim for future work

is to further develop the measurement configuration to achieve a high and constant measurement sensitivity and linearity. A possible alternative for the measurement configuration would be the electrode configuration introduced by Seppä et al. [126], where measurement electrodes are located horizontally on the thorax and the arms in the proximity of the axilla.

Further, multiple-channel bioimpedance [136, 152] as well as EIT [57] and magnetic induction tomography [137] techniques have been introduced for more precise measurements of the dynamic electrical properties of the thorax. However, as these methods either require multiple measurement electrodes, possibly around the chest of the patient, or considerable modifications to the scanner in terms of inductive coils, these methods may not be attractive for clinical use. Despite the complexity of the measurement set-up, Pengpan et al. [115] have introduced EIT in motion compensation during cone-beam CT image acquisition.

Amplitude and time gating methods were compared in study **III**. Amplitude gating showed larger compensation of SUV_{peak} and TBR compared to time gating, whereas in SUV_{max} and SUV_{vol} time gating resulted in larger compensation. In addition, larger displacement was seen in amplitude gating compared to time gating. Generally, the differences between the gating methods are small and non-significant ($p > 0.05$), except in the measurement of cranial-caudal displacement, in which the mean difference is small (0.8 mm) but significant ($p < 0.05$). Thus, according to these results, neither of the two conventional gating methods has a clear advantage over the other in bioimpedance-based respiratory gating. However, previous reports encourage the use of amplitude gating as different parts of respiratory cycles may be incorrectly binned in the same bin due to varying cycle lengths in time gating, which may lead to overlap of motion in the bins and thus to more blur in the images [38, 139]. Amplitude gating methods may also ensure higher count statistics and thus also a higher SNR, as the bin of interest is typically chosen from end-expiration, often the longest and slowest respiratory state. For example, in study **III**,

the five-bin division preserved on average 27% of the data in amplitude gating and 13% in time-based gating. Considering the inversion of the signal, which was encountered with some patients, histogram-based gating methods introduced by Fin et al. [50], Liu et al. [90] and van Elmpt et al. [143] would be very attractive for bioimpedance gating. Histogram methods are robust against signal inversion, since they select the bin according to the count preservation criterion of 35% [143], for example, and minimize the motion within the bin. The drawback of histogram-based gating is that it may require the acquisition of the whole measurement signal before gating and thus prevent prospective gating. On the other hand, according to Didierlaurent et al. [45], retrospective gating should be favoured as it is more robust than prospective gating, which may be based on inaccurate triggering. Triggering inaccuracies have been reported, for example, with the RPM system [45]. Inaccurate triggering may have contributed also to the differences between the bioimpedance and RPM time gating methods seen in study **III**.

An important advantage of the bioimpedance technique is that both bioimpedance-based respiratory gating and ECG-based cardiac gating signals can be acquired simultaneously using the same measurement electrodes. This simple measurement set-up has the potential to facilitate patient preparation and thus to improve work flow. These are important qualities when considering the attractiveness of the method in clinical practice. The use of one set of electrodes minimizes the amount of additional equipment during image acquisition. For example, the presently widely used RPM and Anzai AZ-733 systems require a separate ECG system to enable dual gating. The advantage of the measurement interface (the electrodes) is that it remains attached to the patient during movement. The measurement configuration can thus be set up and tested prior to the radiopharmaceutical injection, although the patient is required to move between preparation and image acquisition. Thus the typically time-consuming patient set-up at the scanner can potentially be shortened, which will reduce the

radiation burden of the employees. Further, the discomfort of the patient due to the measurement interface is assumed to be low since standard ECG electrodes, which patients may already be familiar with, are used in the measurements.

Biopac EBI100C was sufficient for the measurements of the present thesis. However, as the amplifier has some black box solutions which the user cannot modify and as the analysis of its technical properties may be difficult, a logical step would be the development of a specific in-house bioimpedance amplifier. Thus, the occasional baseline drift observed in study **III** could possibly be more frequently avoided. In addition, the 0.05 Hz high-pass filter of the amplifier, which was used in study **IV**, causes a small delay in the measurement signal. Further, online high-pass filtering was found to modify the baseline of the signal in long apnoeic periods and in cases of highly varying respiratory depth. As the results of study **IV** are in line with those of previous studies, the effects of a high-pass filter were not assumed to be significant in this study population. However, the use of an online high-pass filter should be avoided in bioimpedance gating applications.

In addition to PET, the bioimpedance respiratory gating technique, as it is, is applicable in nuclear medicine and CT imaging, which allow retrospective gating. However, if prospective gating is considered, for example in the triggering of CT or linear accelerators, refinements of electrode configuration in terms of sensitivity and linearity as well as of signal processing are recommended. From the electromagnetic compatibility point of view, a systematic study of the compatibility of bioimpedance measurements with implanted electronic devices, such as cardiac pacemakers, should be conducted. This is despite the fact that Kyle et al. [82] have reported that there are no known cases, in which bioimpedance measurements have affected or disturbed cardiac pacemakers. There is demand for a systematic study also in the scientific community [35].

From the gating point of view, a signal-wise comparison of the most typical respiratory measurement methods would be

of interest, since none of the presently widely used methods measures the actual respiratory volume. A majority of the respiratory gating methods studied, except for airway measurement, are based on the monitoring of a surrogate for respiration, typically chest wall motion. Only data-driven methods actually measure the observed respiratory motion. However, these computational methods may not function if sufficient uptake is not present. A comprehensive comparison of different gating methods would thus be very interesting in order to discover the most significant differences between the methods. In this context, it would also be interesting to extensively study the minimum requirements for respiratory motion information to allow effective gating. At the same time, the reproducibility of gating should be precisely defined if gated image sets are used in follow-up studies.

8 Summary and conclusions

In the present thesis, the feasibility of bioimpedance measurements for respiratory and cardiac motion compensation in PET imaging by gating was studied. The thesis includes mathematical modelling, volunteer measurements as well as patient measurements during oncologic and cardiac PET studies.

The main findings of this thesis can be summarized as follows:

I According to the anatomical model, the optimized electrode configuration for the measurement of lung and cardiac volumes is located on the 4th and 5th intercostal spaces contralaterally in the proximity of the mamillae.

II When the optimized electrode configuration is used, the respiratory component of the bioimpedance signal follows the PNT volume spirometry trace accurately.

II When the optimized electrode configuration is used, the cardiac component of the bioimpedance signal has a high temporal association with the ECG measurement. However, due to the occasional suppression of Z peaks, the use of ECG is recommended for cardiac gating.

III/IV Bioimpedance-based respiratory gating was found to effectively detect lesion and myocardium displacement as well as to compensate changes caused by motion in SUV_{peak}, SUV_{max}, SUV_{vol} and TBR in oncologic studies and in myocardial wall thickness in cardiac studies. A minor influence was also observed in left ventricular volume measurements.

III/IV The optimized and II limb lead mimicking electrode configurations are feasible for respiratory gating signal acquisition, but further refinement in terms of measurement sensitivity and linearity is warranted.

IV Bioimpedance-based respiratory gating can be successfully integrated with ECG gating.

References

[1] A. Adler, M. B. Amato, J. H. Arnold, R. Bayford, M. Bodenstein, S. H. Böhm, B. H. Brown, I. Frerichs, O. Stenqvist, N. Weiler and G. K. Wolf, "Whither lung EIT: where are we, where do we want to go and what do we need to get there?" *Physiological Measurement* **33**, 679-694 (2012).

[2] A. Adler, R. Amyot, R. Guardo, J. H. Bates and Y. Berthiaume, "Monitoring changes in lung air and liquid volumes with electrical impedance tomography," *Journal of Applied Physiology* **83**, 1762-1767 (1997).

[3] M. Allen-Auerbach, K. Yeom, J. Park, M. Phelps and J. Czernin, "Standard PET/CT of the chest during shallow breathing is inadequate for comprehensive staging of lung cancer," *Journal of Nuclear Medicine* **47**, 298-301 (2006).

[4] D. Andreuccetti, R. Fossi and C. Petrucci , IFAC-CNR, Florence, Italy, " An internet resource for the calculation of the dielectric properties of body tissues in the frequency range 10 Hz - 100 GHz," *http://niremf.ifac.cnr.it/tissprop/* (2014).

[5] E. Asma, R. Manjeshwar and K. Thielemans, "Theoretical comparison of motion correction techniques for PET image reconstruction," in *Nuclear Science Symposium Conference Record* (IEEE, San Diego, 2006).

[6] E. Atzler and G. Lehmann, "Über ein neues Verfahren zur Darstellung der Herztätigkeit (Dielektrographie)," *Arbeitsphysiologie* **5**, 636-680 (1932).

[7] M. C. Aznar, R. Sersar, J. Saabye, C. N. Ladefoged, F. L. Andersen, J. H. Rasmussen, J. Lofgren and T. Beyer, "Whole-body PET/MRI: the effect of bone attenuation during MR-based

attenuation correction in oncology imaging," *European Journal of Radiology* **83**, 1177-1183 (2014).

[8] W. Bai and M. Brady, "Motion correction and attenuation correction for respiratory gated PET images," *IEEE Transactions on Medical Imaging* **30**, 351-365 (2011).

[9] W. Bai and M. Brady, "Regularized B-spline deformable registration for respiratory motion correction in PET images," *Physics in Medicine and Biology* **54**, 2719-2736 (2009).

[10] L. E. Baker, "Applications of the impedance technique to the respiratory system," *IEEE Engineering in Medicine and Biology Magazine* **8**, 50-52 (1989).

[11] L. E. Baker, L. A. Geddes and H. E. Hoff, "A comparison of linear and non-linear characterizations of impedance spirometry data," *Medical & Biological Engineering* **4**, 371-379 (1966).

[12] L. E. Baker, L. A. Geddes, H. E. Hoff and C. J. Chaput, "Physiological factors underlying transthoracic impedance variations in respiration," *Journal of Applied Physiology* **21**, 1491-1499 (1966).

[13] V. Balasubramanian, O. P. Mathew, A. Behl, S. C. Tewari and R. S. Hoon, "Electrical impedance cardiogram in derivation of systolic time intervals," *British Heart Journal* **40**, 268-275 (1978).

[14] A. S. Beddar, K. Kainz, T. M. Briere, Y. Tsunashima, T. Pan, K. Prado, R. Mohan, M. Gillin and S. Krishnan, "Correlation between internal fiducial tumor motion and external marker motion for liver tumors imaged with 4D-CT," *International Journal of Radiation Oncology, Biology, Physics* **67**, 630-638 (2007).

[15] F. M. Bengel, T. Higuchi, M. S. Javadi and R. Lautamaki, "Cardiac positron emission tomography," *Journal of the American College of Cardiology* **54**, 1-15 (2009).

[16] F. M. Bengel and M. Schwaiger, "PET in Clinical Cardiology" in *Positron Emission Tomography: Clinical Practice*, eds. P.E. Valk, 1st edn, (Springer Verlag, London, 2006), pp. 413-432.

[17] V. Bettinardi, L. Presotto, E. Rapisarda, M. Picchio, L. Gianolli and M. C. Gilardi, "Physical performance of the new hybrid PETCT Discovery-690," *Medical Physics* **38**, 5394-5411 (2011).

[18] BIOPAC Systems Inc , *MP System Hardware Guide,* (Biopac Systems Inc., 42 Aero Camino, Goleta, CA 93117, 17th July 2014).

[19] J. M. Bland and D. G. Altman, "Measuring agreement in method comparison studies," *Statistical Methods in Medical Research* **8**, 135-160 (1999).

[20] M. Blume, A. Martinez-Moller, A. Keil, N. Navab and M. Rafecas, "Joint reconstruction of image and motion in gated positron emission tomography," *IEEE Transactions on Medical Imaging* **29**, 1892-1906 (2010).

[21] A. Böhm and B. L. Heitmann, "The use of bioelectrical impedance analysis for body composition in epidemiological studies," *European Journal of Clinical Nutrition* **67 Suppl 1**, S79-85 (2013).

[22] L. Boucher, S. Rodrigue, R. Lecomte and F. Bénard, "Respiratory gating for 3-dimensional PET of the thorax: Feasibility and initial results," *Journal of Nuclear Medicine* **45**, 214-219 (2004).

[23] J. Bour and J. Kellett, "Impedance cardiography: a rapid and cost-effective screening tool for cardiac disease," *European Journal of Internal Medicine* **19**, 399-405 (2008).

[24] R. A. Bundschuh, A. Martínez-Möller, M. Essler, M. Martínez, S. G. Nekolla, S. I. Ziegler and M. Schwaiger, "Postacquisition detection of tumor motion in the lung and upper abdomen using list-mode PET data: A feasibility study," *Journal of Nuclear Medicine* **48**, 758-763 (2007).

[25] R. A. Bundschuh, N. Andratschke, J. Dinges, M. N. Duma, S. T. Astner, M. Brugel, S. I. Ziegler, M. Molls, M. Schwaiger and M. Essler, "Respiratory gated [18F]FDG PET/CT for target volume delineation in stereotactic radiation treatment of liver metastases," *Strahlentherapie und Onkologie* **188**, 592-598 (2012).

[26] R. A. Bundschuh, A. Martinez-Möller, M. Essler, S. G. Nekolla, S. I. Ziegler and M. Schwaiger, "Local motion correction for lung tumours in PET/CT-first results," *European Journal of Nuclear Medicine and Molecular Imaging* **35**, 1981-1988 (2008).

[27] F. Büther, M. Dawood, L. Stegger, F. Wubbeling, M. Schäfers, O. Schober and K. P. Schäfers, "List mode-driven cardiac and respiratory gating in PET," *Journal of Nuclear Medicine* **50**, 674-681 (2009).

[28] F. Büther, I. Ernst, M. Dawood, P. Kraxner, M. Schäfers, O. Schober and K. P. Schäfers, "Detection of respiratory tumour motion using intrinsic list mode-driven gating in positron emission tomography," *European Journal of Nuclear Medicine and Molecular Imaging* **37**, 2315-2327 (2010).

[29] F. Büther, I. Ernst, J. Hamill, H. T. Eich, O. Schober, M. Schäfers and K. P. Schäfers, "External radioactive markers for PET data-driven respiratory gating in positron emission tomography," *European Journal of Nuclear Medicine and Molecular Imaging* **40**, 602-614 (2013).

[30] K. S. Cheng, D. Isaacson, J. C. Newell and D. G. Gisser, "Electrode models for electric current computed tomography," *IEEE Transactions on Biomedical Engineering* **36**, 918-924 (1989).

[31] V. A. Cherepenin, A. Y. Karpov, A. V. Korjenevsky, V. N. Kornienko, Y. S. Kultiasov, M. B. Ochapkin, O. V. Trochanova and J. D. Meister, "Three-dimensional EIT imaging of breast tissues: system design and clinical testing," *IEEE Transactions on Medical Imaging* **21**, 662-667 (2002).

[32] S. R. Cherry, J. A. Sorenson and M. E. Phelps, *Physics in Nuclear Medicine*. 3rd edn. (Saunders, Philadelphia, 2003).

[33] K. Cho, S. Kumiata, S. Okada and T. Kumazaki, "Development of respiratory gated myocardial SPECT system," *Journal of Nuclear Cardiology* **6**, 20-28 (1999).

[34] A. J. Cole, G. G. Hanna, S. Jain and J. M. O'Sullivan, "Motion management for radical radiotherapy in non-small cell lung cancer," *Clinical Oncology* **26**, 67-80 (2014).

[35] R. Conwell, C. Bai, J. Kindem, H. Babla, D. Solis, R. De Los Santos and M. Gurley, "An Operator-Passive Thoracic Impedance Approach for Respiratory Motion Gating in Myocardial Perfusion SPECT," in *IEEE Nuclear Science Symposium Conference Record* (IEEE, 2011).

[36] G. J. R. Cook, "Artifacts and Normal Variant in Whole-Body PET and PET/CT Imaging" in *Positron Emission Tomography: Clinical Practice*, eds. P.E. Valk, 1st edn, (Springer Verlag, London, 2006), pp. 63-77.

[37] B. D. Coombs, J. Szumowski and W. Coshow, "Two-point Dixon technique for water-fat signal decomposition with B0 inhomogeneity correction," *Magnetic Resonance in Medicine* **38**, 884-889 (1997).

[38] M. Dawood, F. Büther, N. Lang, O. Schober and K. P. Schäfers, "Respiratory gating in positron emission tomography: a quantitative comparison of different gating schemes," *Medical Physics* **34**, 3067-3076 (2007).

[39] M. Dawood, T. Kösters, M. Fieseler, F. Büther, X. Jiang, F. Wubbeling and K. P. Schäfers, "Motion correction in respiratory gated cardiac PET/CT using multi-scale optical flow," *MICCAI International Conference on Medical Image Computing and Computer-Assisted Intervention* **11**, 155-162 (2008).

[40] M. Defrise and P. E. Kinahan, "Data Acquisition and Image Reconstruction for 3D PET" in *The Theory and Practice of 3D PET*, eds. B. Bendriem and D.W. Townsend, 1st edn, (Kluwer Academic Publishers, Dordrecht, 2003), pp. 11-54.

[41] M. Defrise, A. Rezaei and J. Nuyts, "Time-of-flight PET data determine the attenuation sinogram up to a constant," *Physics in Medicine and Biology* **57**, 885-899 (2012).

[42] J. M. Deibele, H. Luepschen and S. Leonhardt, "Dynamic separation of pulmonary and cardiac changes in electrical impedance tomography," *Physiological Measurement* **29**, S1-14 (2008).

[43] G. Delso, A. Martinez-Möller, R. A. Bundschuh, S. G. Nekolla, S. I. Ziegler and M. Schwaiger, "Preliminary study of the detectability of coronary plaque with PET," *Physics in Medicine and Biology* **56**, 2145-2160 (2011).

[44] J. C. Dickson, C. O'Meara and A. Barnes, "A comparison of CT- and MR-based attenuation correction in neurological PET," *European Journal of Nuclear Medicine and Molecular Imaging* **41**, 1176-1189 (2014).

[45] D. Didierlaurent, S. Ribes, H. Batatia, C. Jaudet, L. O. Dierickx, S. Zerdoud, S. Brillouet, O. Caselles and F. Courbon, "The retrospective binning method improves the consistency of phase binning in respiratory-gated PET/CT," *Physics in Medicine and Biology* **57**, 7829-7841 (2012).

[46] D. Didierlaurent, S. Ribes, O. Caselles, C. Jaudet, J. M. Cazalet, H. Batatia and F. Courbon, "A new respiratory gating device to improve 4D PET/CT," *Medical Physics* **40**, 032501 (2013).

[47] Y. E. Erdi, S. A. Nehmeh, T. Pan, A. Pevsner, K. E. Rosenzweig, G. Mageras, E. D. Yorke, H. Schoder, W. Hsiao, O. D. Squire, P. Vernon, J. B. Ashman, H. Mostafavi, S. M. Larson and J. L. Humm, "The CT motion quantitation of lung lesions and its

impact on PET-measured SUVs," *Journal of Nuclear Medicine* **45**, 1287-1292 (2004).

[48] J. M. Ernst, D. A. Litvack, D. L. Lozano, J. T. Cacioppo and G. G. Berntson, "Impedance pneumography: noise as signal in impedance cardiography," *Psychophysiology* **36**, 333-338 (1999).

[49] L. Fin, P. Bailly, J. Daouk and M. E. Meyer, "Motion correction based on an appropriate system matrix for statistical reconstruction of respiratory-correlated PET acquisitions," *Computer Methods and Programs in Biomedicine* **96**, e1-9 (2009).

[50] L. Fin, J. Daouk, J. Morvan, P. Bailly, I. El Esper, L. Saidi and M. E. Meyer, "Initial clinical results for breath-hold CT-based processing of respiratory-gated PET acquisitions," *European Journal of Nuclear Medicine and Molecular Imaging* **35**, 1971-1980 (2008).

[51] R. D. Finn and D. J. Schlyer, "Production of Radionuclides for PET" in *Principles and Practice of Positron Emission Tomography*, eds. R.L. Wahl and J.W. Buchanan, 1st edn, (Lippincott Williams & Wilkins, Philadelphia, PA, USA, 2002), pp. 1-15.

[52] J. J. Freundlich and J. C. Erickson, "Electrical impedance pneumography for simple nonrestrictive continuous monitoring of respiratory rate, rhythm and tidal volume for surgical patients," *Chest* **65**, 181-184 (1974).

[53] S. Gabriel, R. W. Lau and C. Gabriel, "The dielectric properties of biological tissues: III. Parametric models for the dielectric spectrum of tissues," *Physics in Medicine and Biology* **41**, 2271-2293 (1996).

[54] D. P. Gierga, J. Brewer, G. C. Sharp, M. Betke, C. G. Willett and G. T. Chen, "The correlation between internal and external markers for abdominal tumors: implications for respiratory gating," *International Journal of Radiation Oncology, Biology, Physics* **61**, 1551-1558 (2005).

[55] F. Gigengack, L. Ruthotto, M. Burger, C. H. Wolters, X. Jiang and K. P. Schafers, "Motion correction in dual gated cardiac PET using mass-preserving image registration," *IEEE Transactions on Medical Imaging* **31**, 698-712 (2012).

[56] E. S. Goldensohn and L. Zablow, "An electrical impedance spirometer," *Journal of Applied Physiology* **14**, 463-464 (1959).

[57] C. A. Grant, T. Pham, J. Hough, T. Riedel, C. Stocker and A. Schibler, "Measurement of ventilation and cardiac related impedance changes with electrical impedance tomography," *Critical Care* **15**, R37 (2011).

[58] S. Grimnes and Ø G. Martinsen, *Bioimpedance and Bioelectricity Basics,* 2nd edn. (Academic Press, Oxford, 2008).

[59] A. C. Guyton and J. E. Hall, *Textbook of Medical Physiology,* 11th edn. (Elsevier, Philadelphia, 2006).

[60] E. Haug, O. Sand, O. V. Sjaastad and K. C. Toverud, *Ihmisen fysiologia,* 1st-2nd edn. (WSOY, Porvoo, 1999).

[61] J. He, G.J. O'Keefe, T. Ackerly and M. Geso, "Respiratory motion gating based on list-mode data in 3D PET: A simulation study using the dynamic NCAT phantom," in *The 1st International Conference on Information Science and Engineering* (IEEE, Nanjing, 2009).

[62] M. Hofmann, F. Steinke, V. Scheel, G. Charpiat, J. Farquhar, P. Aschoff, M. Brady, B. Scholkopf and B. J. Pichler, "MRI-based attenuation correction for PET/MRI: a novel approach combining pattern recognition and atlas registration," *Journal of Nuclear Medicine* **49**, 1875-1883 (2008).

[63] J. D. Hoisak, K. E. Sixel, R. Tirona, P. C. Cheung and J. P. Pignol, "Correlation of lung tumor motion with external surrogate indicators of respiration," *International Journal of Radiation Oncology, Biology, Physics* **60**, 1298-1306 (2004).

[64] J. H. Houtveen, P. F. Groot and E. J. de Geus, "Validation of the thoracic impedance derived respiratory signal using multilevel analysis," *International Journal of Psychophysiology* **59**, 97-106 (2006).

[65] D. Ionascu, S. B. Jiang, S. Nishioka, H. Shirato and R. I. Berbeco, "Internal-external correlation investigations of respiratory induced motion of lung tumors," *Medical Physics* **34**, 3893-3903 (2007).

[66] A. A. Jackson, M. Johnson, K. Durkin and S. Wootton, "Body composition assessment in nutrition research: value of BIA technology," *European Journal of Clinical Nutrition* **67 Suppl 1**, S71-8 (2013).

[67] M. W. Jacobson and J. A. Fessler, "Joint estimation of image and deformation parameters in motion-corrected PET," *IEEE Nuclear Science Symposium Conference Record 2003* **5**, 3290-3294 (2003).

[68] B. W. Jakoby, Y. Bercier, M. Conti, M. E. Casey, B. Bendriem and D. W. Townsend, "Physical and clinical performance of the mCT time-of-flight PET/CT scanner," *Physics in Medicine and Biology* **56**, 2375-2389 (2011).

[69] R. L. Jones and M. M. Nzekwu, "The effects of body mass index on lung volumes," *Chest* **130**, 827-833 (2006).

[70] P. K. Kauppinen, J. A. Hyttinen, T. Koobi and J. Malmivuo, "Lead field theoretical approach in bioimpedance measurements: towards more controlled measurement sensitivity," *Annals of the New York Academy of Sciences* **873**, 135-142 (1999).

[71] T. Kawano, E. Ohtake and T. Inoue, "Deep-inspiration breath-hold PET/CT of lung cancer: maximum standardized uptake value analysis of 108 patients," *Journal of Nuclear Medicine* **49**, 1223-1231 (2008).

[72] V. Keereman, Y. Fierens, T. Broux, Y. De Deene, M. Lonneux and S. Vandenberghe, "MRI-based attenuation correction for PET/MRI

using ultrashort echo time sequences," *Journal of Nuclear Medicine* **51**, 812-818 (2010).

[73] A. L. Kesner and C. Kuntner, "A new fast and fully automated software based algorithm for extracting respiratory signal from raw PET data and its comparison to other methods," *Medical Physics* **37**, 5550-5559 (2010).

[74] J. H. Killoran, V. H. Gerbaudo, M. Mamede, D. Ionascu, S. J. Park and R. Berbeco, "Motion artifacts occurring at the lung/diaphragm interface using 4D CT attenuation correction of 4D PET scans," *Journal of Applied Clinical Medical Physics* **12**, 3502 (2011).

[75] K. Kitamura, H. Shirato, Y. Seppenwoolde, T. Shimizu, Y. Kodama, H. Endo, R. Onimaru, M. Oda, K. Fujita, S. Shimizu and K. Miyasaka, "Tumor location, cirrhosis, and surgical history contribute to tumor movement in the liver, as measured during stereotactic irradiation using a real-time tumor-tracking radiotherapy system," *International Journal of Radiation Oncology, Biology, Physics* **56**, 221-228 (2003).

[76] G. J. Klein, B. W. Reutter, M. H. Ho, J. H. Reed and R. H. Huesman, "Real-time system for respiratory-cardiac gating in positron tomography," *IEEE Transaction on Nuclear Science* **45**, 2139-2143 (1998).

[77] G. J. Klein, B. W. Reutter and R. H. Huesman, "Non-rigid summing of gated PET via optical flow," *IEEE Transaction on Nuclear Science* **44**, 1509-1512 (1997).

[78] G. J. Klein and R. H. Huesman, "Four-dimensional processing of deformable cardiac PET data," *Medical Image Analysis* **6**, 29-46 (2002).

[79] N. Koch, H. H. Liu, G. Starkschall, M. Jacobson, K. Forster, Z. Liao, R. Komaki and C. W. Stevens, "Evaluation of internal lung motion for respiratory-gated radiotherapy using MRI: Part I-

correlating internal lung motion with skin fiducial motion," *International Journal of Radiation Oncology, Biology, Physics* **60**, 1459-1472 (2004).

[80] T. Kokki, H. T. Sipila, M. Teras, T. Noponen, N. Durand-Schaefer, R. Klen and J. Knuuti, "Dual gated PET/CT imaging of small targets of the heart: method description and testing with a dynamic heart phantom," *Journal of Nuclear Cardiology* **17**, 71-84 (2010).

[81] W. G. Kubicek, R. P. Patterson and D. A. Witsoe, "Impedance cardiography as a noninvasive method of monitoring cardiac function and other parameters of the cardiovascular system," *Annals of the New York Academy of Sciences* **170**, 724-732 (1970).

[82] U. G. Kyle, I. Bosaeus, A. D. De Lorenzo, P. Deurenberg, M. Elia, J. Manuel Gomez, B. Lilienthal Heitmann, L. Kent-Smith, J. C. Melchior, M. Pirlich, H. Scharfetter, A. M W J Schols, C. Pichard and ESPEN, "Bioelectrical impedance analysis-part II: utilization in clinical practice," *Clinical Nutrition* **23**, 1430-1453 (2004).

[83] Z. Lababidi, D. A. Ehmke, R. E. Durnin, P. E. Leaverton and R. M. Lauer, "The first derivative thoracic impedance cardiogram," *Circulation* **41**, 651-658 (1970).

[84] F. Lamare, T. Cresson, J. Savean, C. Cheze Le Rest, A. J. Reader and D. Visvikis, "Respiratory motion correction for PET oncology applications using affine transformation of list mode data," *Physics in Medicine and Biology* **52**, 121-140 (2007).

[85] F. Lamare, M. J. Ledesma Carbayo, T. Cresson, G. Kontaxakis, A. Santos, C. C. Le Rest, A. J. Reader and D. Visvikis, "List-mode-based reconstruction for respiratory motion correction in PET using non-rigid body transformations," *Physics in Medicine and Biology* **52**, 5187-5204 (2007).

[86] P. Lee, P. Kupelian, J. Czernin and P. Ghosh, "Current concepts in F18 FDG PET/CT-based radiation therapy planning for lung cancer," *Frontiers in Oncology* **2**, 71 (2012).

[87] T. Lewellen and J. Karp, "PET Systems" in *Emission Tomography: The Fundamentals of PET and SPECT*, eds. M.N. Wernick and J.N. Aarsvold, 1st edn, (Elsevier Academic Press, London, 2004), pp. 179-194.

[88] B. E. Lingwood, "Bioelectrical impedance analysis for assessment of fluid status and body composition in neonates--the good, the bad and the unknown," *European Journal of Clinical Nutrition* **67 Suppl 1**, S28-33 (2013).

[89] C. Liu, L. A. I. Pierce, A. M. Alessio and P. E. Kinahan, "The impact of respiratory motion on tumor quantification and delineation in static PET/CT imaging," *Physics in Medicine and Biology* **54**, 7345-7362 (2009).

[90] C. Liu, A. Alessio, L. Pierce, K. Thielemans, S. Wollenweber, A. Ganin and P. Kinahan, "Quiescent period respiratory gating for PET/CT," *Medical Physics* **37**, 5037-5043 (2010).

[91] L. Livieratos, K. Rajappan, L. Stegger, K. Schafers, D. L. Bailey and P. G. Camici, "Respiratory gating of cardiac PET data in list-mode acquisition," *European Journal of Nuclear Medicine and Molecular Imaging* **33**, 584-588 (2006).

[92] J. L. Logic, M. G. Maksud and L. H. Hamilton, "Factors affecting transthoracic impedance signals used to measure breathing," *Journal of Applied Physiology* **22**, 251-254 (1967).

[93] S. Luo, V. X. Afonso, J. G. Webster and W. J. Tompkins, "The electrode system in impedance-based ventilation measurement," *IEEE Transactions on Biomedical Engineering* **39**, 1130-1141 (1992).

[94] J. Malmivuo and R. Plonsey, *Bioelectromagnetism: Principles and Applications of Bioelectric and Biomagnetic Fields,* 1st edn. (Oxford University Press, New York, 1995).

[95] A. Martinez-Moller, M. Souvatzoglou, G. Delso, R. A. Bundschuh, C. Chefd'hotel, S. I. Ziegler, N. Navab, M. Schwaiger and S. G. Nekolla, "Tissue classification as a potential approach for attenuation correction in whole-body PET/MRI: evaluation with PET/CT data," *Journal of Nuclear Medicine* **50**, 520-526 (2009).

[96] A. Martinez-Möller, D. Zikic, R. M. Botnar, R. A. Bundschuh, W. Howe, S. I. Ziegler, N. Navab, M. Schwaiger and S. G. Nekolla, "Dual cardiac-respiratory gated PET: implementation and results from a feasibility study," *European Journal of Nuclear Medicine and Molecular Imaging* **34**, 1447-1454 (2007).

[97] R. E. Mason and I. Likar, "A new system of multiple-lead exercise electrocardiography," *American Heart Journal* **71**, 196-205 (1966).

[98] G. S. Meirelles, Y. E. Erdi, S. A. Nehmeh, O. D. Squire, S. M. Larson, J. L. Humm and H. Schoder, "Deep-inspiration breath-hold PET/CT: clinical findings with a new technique for detection and characterization of thoracic lesions," *Journal of Nuclear Medicine* **48**, 712-719 (2007).

[99] K. Mitsumoto, K. Abe, Y. Sakaguchi, T. Zhang, Y. Tachiya, N. Ohya, S. Baba and M. Sasaki, "Determination of the optimal acquisition protocol of breath-hold PET/CT for the diagnosis of thoracic lesions," *Nuclear Medicine Communications* **32**, 1148-1154 (2011).

[100] J. R. Moon, "Body composition in athletes and sports nutrition: an examination of the bioimpedance analysis technique," *European Journal of Clinical Nutrition* **67 Suppl 1**, S54-9 (2013).

[101] M. Mori, K. Murata, M. Takahashi, K. Shimoyama, T. Ota, R. Morita and T. Sakamoto, "Accurate contiguous sections without breath-holding on chest CT: value of respiratory gating and

ultrafast CT," *AJR. American Journal of Roentgenology* **162**, 1057-1062 (1994).

[102] S. Nagamachi, H. Wakamatsu, S. Kiyohara, S. Fujita, S. Futami, H. Arita, R. Nishii, S. Tamura and K. Kawai, "Usefulness of a deep-inspiration breath-hold 18F-FDG PET/CT technique in diagnosing liver, bile duct, and pancreas tumors," *Nuclear Medicine Communications* **30**, 326-332 (2009).

[103] National Electrical Manufacturers Association, *NEMA NU 2-2007 Performance Measurements of Positron Emission Tomographs*, (National Electrical Manufacturers Association, Rosslyn, VA, 2007).

[104] B. K. Navalpakkam, H. Braun, T. Kuwert and H. H. Quick, "Magnetic resonance-based attenuation correction for PET/MR hybrid imaging using continuous valued attenuation maps," *Investigative Radiology* **48**, 323-332 (2013).

[105] S. A. Nehmeh, Y. E. Erdi, C. C. Ling, K. E. Rosenzweig, H. Schoder, S. M. Larson, H. A. Macapinlac, O. D. Squire and J. L. Humm, "Effect of respiratory gating on quantifying PET images of lung cancer," *Journal of Nuclear Medicine* **43**, 876-881 (2002).

[106] S. A. Nehmeh and Y. E. Erdi, "Respiratory motion in positron emission tomography/computed tomography: a review," *Seminars in Nuclear Medicine* **38**, 167-176 (2008).

[107] S. A. Nehmeh, Y. E. Erdi, G. S. Meirelles, O. Squire, S. M. Larson, J. L. Humm and H. Schoder, "Deep-inspiration breath-hold PET/CT of the thorax," *Journal of Nuclear Medicine* **48**, 22-26 (2007).

[108] P. L. Nunez and R. Srinivasan, *Electric Fields of the Brain the Neurophysics of EEG*, 2nd edn. (Oxford University Press, New York, 2006).

[109] J. Nyboer, "Electrical impedance plethysmography; a physical and physiologic approach to peripheral vascular study," *Circulation* **2**, 811-821 (1950).

[110] Y. Otani, I. Fukuda, N. Tsukamoto, Y. Kumazaki, H. Sekine, E. Imabayashi, O. Kawaguchi, T. Nose, T. Teshima and T. Dokiya, "A comparison of the respiratory signals acquired by different respiratory monitoring systems used in respiratory gated radiotherapy," *Medical Physics* **37**, 6178-6186 (2010).

[111] J. Pan and W. J. Tompkins, "A real-time QRS detection algorithm," *IEEE Transactions on Biomedical Engineering* **32**, 230-236 (1985).

[112] T. Pan, O. Mawlawi, S. A. Nehmeh, Y. E. Erdi, D. Luo, H. H. Liu, R. Castillo, R. Mohan, Z. Liao and H. A. Macapinlac, "Attenuation correction of PET images with respiration-averaged CT images in PET/CT," *Journal of Nuclear Medicine* **46**, 1481-1487 (2005).

[113] R. P. Patterson, "Fundamentals of impedance cardiography," *IEEE Engineering in Medicine and Biology Magazine* **8**, 35-38 (1989).

[114] R. P. Patterson, "Sources of the thoracic cardiogenic electrical impedance signal as determined by a model," *Medical & Biological Engineering & Computing* **23**, 411-417 (1985).

[115] T. Pengpan, N. D. Smith, W. Qiu, A. Yao, C. N. Mitchell and M. Soleimani, "A motion-compensated cone-beam CT using electrical impedance tomography imaging," *Physiological Measurement* **32**, 19-34 (2011).

[116] M. E. Phelps, S. R. Cherry and M. Dahlbom, *PET Physics, Instrumentation and Scanners,* 1st edn. (Springer, New York, 2010).

[117] C. Plathow, S. Ley, C. Fink, M. Puderbach, W. Hosch, A. Schmahl, J. Debus and H. U. Kauczor, "Analysis of intrathoracic tumor mobility during whole breathing cycle by dynamic MRI," *International Journal of Radiation Oncology, Biology, Physics* **59**, 952-959 (2004).

[118] I. Polycarpou, C. Tsoumpas and P. K. Marsden, "Analysis and comparison of two methods for motion correction in PET imaging," *Medical Physics* **39**, 6474-6483 (2012).

[119] J. Prekeges, *Nuclear Medicine Instrumentation,* 1st edn. (Jones and Bartlett Publishers, Sudbury, 2011).

[120] F. P. J. Primiano, "Measurements of the Respiratory System" in *Medical Instrumentation: Application and Design*, eds. J.G. Webster, 2nd edn. (Houghton Mifflin Company, Boston, 1992), pp. 457-539.

[121] A. Rahmim, T. Jing, M.R. Ay and F.M. Bengel, "4D respiratory motion-corrected Rb-82 myocardial perfusion PET image reconstruction," in *Nuclear Science Symposium Conference Record (NSS/MIC), 2010 IEEE* (IEEE, 2010).

[122] O. Riou, B. Serrano, D. Azria, B. Paulmier, R. Villeneuve, P. Fenoglietto, A. Artenie, C. Ortholan, M. Faraggi and J. Thariat, "Integrating respiratory-gated PET-based target volume delineation in liver SBRT planning, a pilot study," *Radiation Oncology* **9**, 127-717X-9-127 (2014).

[123] A. V. Sahakian, W. J. Tompkins and J. G. Webster, "Electrode motion artifacts in electrical impedance pneumography," *IEEE Transactions on Biomedical Engineering* **32**, 448-451 (1985).

[124] P. J. Schleyer, M. J. O'Doherty, S. F. Barrington and P. K. Marsden, "Retrospective data-driven respiratory gating for PET/CT," *Physics in Medicine and Biology* **54**, 1935-1950 (2009).

[125] P. J. Schleyer, M. J. O'Doherty and P. K. Marsden, "Extension of a data-driven gating technique to 3D, whole body PET studies," *Physics in Medicine and Biology* **56**, 3953-3965 (2011).

[126] V. P. Seppä, J. Hyttinen, M. Uitto, W. Chrapek and J. Viik, "Novel electrode configuration for highly linear impedance pneumography," *Biomedizinische Technik.Biomedical engineering* **58**, 35-38 (2013).

[127] V. P. Seppä, J. Hyttinen and J. Viik, "A method for suppressing cardiogenic oscillations in impedance pneumography," *Physiological Measurement* **32**, 337-345 (2011).

[128] V. P. Seppä, A. S. Pelkonen, A. Kotaniemi-Syrjänen, M. J. Mäkelä, J. Viik and L. P. Malmberg, "Tidal breathing flow measurement in awake young children by using impedance pneumography," *Journal of Applied Physiology* **115**, 1725-1731 (2013).

[129] V. P. Seppä, J. Viik and J. Hyttinen, "Assessment of pulmonary flow using impedance pneumography," *IEEE Transactions on Biomedical Engineering* **57**, 2277-2285 (2010).

[130] Y. Seppenwoolde, H. Shirato, K. Kitamura, S. Shimizu, M. van Herk, J. V. Lebesque and K. Miyasaka, "Precise and real-time measurement of 3D tumor motion in lung due to breathing and heartbeat, measured during radiotherapy," *International Journal of Radiation Oncology, Biology, Physics* **53**, 822-834 (2002).

[131] C. Shah, S. Badiyan, S. Berry, A. J. Khan, S. Goyal, K. Schulte, A. Nanavati, M. Lynch and F. A. Vicini, "Cardiac dose sparing and avoidance techniques in breast cancer radiotherapy," *Radiotherapy and Oncology* (2014).

[132] G. Shechter, C. Ozturk, J. R. Resar and E. R. McVeigh, "Respiratory motion of the heart from free breathing coronary angiograms," *IEEE Transactions on Medical Imaging* **23**, 1046-1056 (2004).

[133] P. D. Shreve "PET and PET/CT Imaging in Urologic Tumours" in *Positron Emission Tomography: Clinical Practice*, eds. P.E. Valk, 1st edn. (Springer Verlag, London, 2006), pp. 243-251.

[134] E. Somersalo, M. Cheney and D. Isaacson, "Existence and uniqueness for electrode models for electric current computed tomography," *SIAM Journal on Applied Mathematics* **52**, 1023-1040 (1992).

[135] M. Soret, S. L. Bacharach and I. Buvat, "Partial-volume effect in PET tumor imaging," *Journal of Nuclear Medicine* **48**, 932-945 (2007).

[136] A. W. Stanley Jr, J. W. Herald, C. L. Athanasuleas, S. C. Jacob, A. A. Bartolucci and A. N. Tsoglin, "Multi-channel electrical bioimpedance: a non-invasive method to simultaneously measure cardiac output and individual arterial limb flow in patients with cardiovascular disease," *Journal of Clinical Monitoring and Computing* **23**, 243-251 (2009).

[137] M. Steffen, A. Aleksandrowicz and S. Leonhardt, "Mobile noncontact monitoring of heart and lung activity," *IEEE Transactions on Biomedical Circuits and Systems* **1**, 250-257 (2007).

[138] L. G. Strauss and P. S. Conti, "The applications of PET in clinical oncology," *Journal of Nuclear Medicine* **32**, 623-48; discussion 649-50 (1991).

[139] B. K. Teo, B. Saboury, R. Munbodh, J. Scheuermann, D. A. Torigian, H. Zaidi and A. Alavi, "The effect of breathing irregularities on quantitative accuracy of respiratory gated PETCT," *Medical Physics* **39**, 7390-7397 (2012).

[140] M. Teräs, T. Kokki, N. Durand-Schaefer, T. Noponen, M. Pietilä, J. Kiss, E. Hoppela, H. T. Sipilä and J. Knuuti, "Dual-gated cardiac PET-Clinical feasibility study," *European Journal of Nuclear Medicine and Molecular Imaging* **37**, 505-516 (2010).

[141] M. M. Ter-Pogossian, S. R. Bergmann and B. E. Sobel, "Influence of cardiac and respiratory motion on tomographic reconstructions of the heart: implications for quantitative nuclear cardiology," *Journal of Computer Assisted Tomography* **6**, 1148-1155 (1982).

[142] T. Torizuka, Y. Tanizaki, T. Kanno, M. Futatsubashi, E. Yoshikawa, H. Okada and Y. Ouchi, "Single 20-second acquisition of deep-inspiration breath-hold PET/CT: clinical feasibility for lung cancer," *Journal of Nuclear Medicine* **50**, 1579-1584 (2009).

[143] W. van Elmpt, J. Hamill, J. Jones, D. De Ruysscher, P. Lambin and M. Ollers, "Optimal gating compared to 3D and 4D PET reconstruction for characterization of lung tumours," *European Journal of Nuclear Medicine and Molecular Imaging* **38**, 843-855 (2011).

[144] M. Vauhkonen, *Electrical Impedance Tomography and Prior Information,* Doctoral Dissertation (Kuopio University Printing Office, 1997).

[145] M. Vauhkonen, W. R. Lionheart, L. M. Heikkinen, P. J. Vauhkonen and J. P. Kaipio, "A MATLAB package for the EIDORS project to reconstruct two-dimensional EIT images," *Physiological Measurement* **22**, 107-111 (2001).

[146] M. Vauhkonen, D. Vadasz, P. A. Karjalainen, E. Somersalo and J. P. Kaipio, "Tikhonov regularization and prior information in electrical impedance tomography," *IEEE Transactions on Medical Imaging* **17**, 285-293 (1998).

[147] P. J. Vauhkonen, M. Vauhkonen, T. Savolainen and J. P. Kaipio, "Three-dimensional electrical impedance tomography based on the complete electrode model," *IEEE Transactions on Biomedical Engineering* **46**, 1150-1160 (1999).

[148] J. A. Victorino, J. B. Borges, V. N. Okamoto, G. F. Matos, M. R. Tucci, M. P. Caramez, H. Tanaka, F. S. Sipmann, D. C. Santos, C. S. Barbas, C. R. Carvalho and M. B. Amato, "Imbalances in regional lung ventilation: a validation study on electrical impedance tomography," *American Journal of Respiratory and Critical Care medicine* **169**, 791-800 (2004).

[149] T. Vilhunen, J. P. Kaipio, P. J. Vauhkonen, T. Savolainen and M. Vauhkonen, "Simultaneous reconstruction of electrode contact impedances and internal electrical properties: I. Theory," *Measurement Science and Technology* **13**, 1848-1854 (2002).

[150] I. Virgolini, V. Ambrosini, J. B. Bomanji, R. P. Baum, S. Fanti, M. Gabriel, N. D. Papathanasiou, G. Pepe, W. Oyen, C. De Cristoforo and A. Chiti, "Procedure guidelines for PET/CT tumour imaging with 68Ga-DOTA-conjugated peptides: 68Ga-DOTA-TOC, 68Ga-DOTA-NOC, 68Ga-DOTA-TATE," *European Journal of Nuclear Medicine and Molecular Imaging* **37**, 2004-2010 (2010).

[151] D. Visvikis, F. Monnier, J. Bert, M. Hatt and H. Fayad, "PET/MR attenuation correction: where have we come from and where are we going?" *European Journal of Nuclear Medicine and Molecular Imaging* **41**, 1172-1175 (2014).

[152] V. Vondra, J. Halamek, I. Viscor and P. Jurak, "Two-channel bioimpedance monitor for impedance cardiography," *Conference proceedings: Annual International Conference of the IEEE Engineering in Medicine and Biology Society. IEEE Engineering in Medicine and Biology Society.Conference* **1**, 6061-6063 (2006).

[153] R. L. Wahl, H. Jacene, Y. Kasamon and M. A. Lodge, "From RECIST to PERCIST: Evolving Considerations for PET response criteria in solid tumors," *Journal of Nuclear Medicine* **50 Suppl 1**, 122S-50S (2009).

[154] Y. Wang, E. Vidan and G. W. Bergman, "Cardiac motion of coronary arteries: variability in the rest period and implications for coronary MR angiography," *Radiology* **213**, 751-758 (1999).

[155] C. C. Watson, D. W. Townsend and B. Bendriem, "PET/CT Systems" in *Emission Tomography: The Fundamentals of PET and SPECT*, eds. M.N. Wernick and J.N. Aarsvold, 1st edn. (Elsevier Academic Press, London, 2004), pp. 195-212.

[156] W. A. Weber, S. I. Ziegler, R. Thodtmann, A. R. Hanauske and M. Schwaiger, "Reproducibility of metabolic measurements in malignant tumors using FDG PET," *Journal of Nuclear Medicine* **40**, 1771-1777 (1999).

[157] M.N. Wernick & J.N. Aarsvold, "Introduction to emission tomography" in *Emission Tomography: The Fundamentals of PET and SPECT*, eds. M.N. Wernick and J.N. Aarsvold, 1st edn, (Elsevier Academic Press, London, 2004), pp. 11-24.

[158] J. W. Wolthaus, M. van Herk, S. H. Muller, J. S. Belderbos, J. V. Lebesque, J. A. de Bois, M. M. Rossi and E. M. Damen, "Fusion of respiration-correlated PET and CT scans: correlated lung tumour motion in anatomical and functional scans," *Physics in Medicine and Biology* **50**, 1569-1583 (2005).

[159] T. Z. Wong and R. E. Coleman, "PET Imaing in Brain Tumors" in *Positron Emission Tomography: Clinical Practice*, eds. P.E. Valk, 1st edn, (Springer Verlag, London, 2006), pp. 79-88.

[160] T. Yamaguchi, O. Ueda, H. Hara, H. Sakai, T. Kida, K. Suzuki, S. Adachi and K. Ishii, "Usefulness of a breath-holding acquisition method in PET/CT for pulmonary lesions," *Annals of Nuclear Medicine* **23**, 65-71 (2009).

[161] G. Youssef, R. S. Beanlands, D. H. Birnie and P. B. Nery, "Cardiac sarcoidosis: applications of imaging in diagnosis and directing treatment," *Heart* **97**, 2078-2087 (2011).

[162] H. Zhuang and A. Alavi, "Evolving Role of FDG-PET Imaging in the Management of Patients with Suspected Infection and Inflammatory Disorders" in *Positron Emission Tomography: Clinical Practice*, eds. P.E. Valk, 1st edn. (Springer Verlag, London, 2006), pp. 303-316.

[163] S. Zlochiver, M. Arad, M. M. Radai, D. Barak-Shinar, H. Krief, T. Engelman, R. Ben-Yehuda, A. Adunsky and S. Abboud, "A portable bio-impedance system for monitoring lung resistivity," *Medical Engineering & Physics* **29**, 93-100 (2007).

Tuomas Koivumäki

The Bioimpedance Technique in Respiratory- and Dual-Gated Positron Emission Tomography Imaging

Respiratory and cardiac motion artefacts degrade image quality in positron emission tomography imaging and may significantly affect the qualitative and quantitative evaluation of images. At worst, misguided interpretation may lead to wrong diagnosis and inadequate or unnecessary treatment. Thus, effective methods to compensate the adverse effects of motion are called for in clinical practice. This thesis shows that bioimpedance techniques can be effectively utilized for respiratory motion compensation by respiratory and dual gating of oncologic and cardiac PET imaging.

UNIVERSITY OF
EASTERN FINLAND

Publications of the University of Eastern Finland
Dissertations in Forestry and Natural Sciences

ISBN 978-952-61-1580-1